Resolvent-based modeling of coherent wave packets in a turbulent jet

Lutz Lesshafft,[1] Onofrio Semeraro,[1,2] Vincent Jaunet,[3] André V. G. Cavalieri,[4] and Peter Jordan[3]

[1]*Laboratoire d'Hydrodynamique, CNRS/École polytechnique, 91120 Palaiseau, France*
[2]*LIMSI, CNRS/Université Paris-Saclay, 91400 Orsay, France*
[3]*Institut Pprime, CNRS/Université de Poitiers/ENSMA, 86962 Futuroscope Chasseneuil, France*
[4]*Divisão de Engenharia Aeronáutica, Instituto Tecnológico de Aeronáutica,*
São José dos Campos, 12228-900 São Paulo, Brazil

Coherent turbulent wave-packet structures in a jet at Reynolds number 460 000 and Mach number 0.4 are extracted from experimental measurements and are modeled as linear fluctuations around the mean flow. The linear model is based on harmonic optimal forcing structures and their associated flow response at individual Strouhal numbers, obtained from analysis of the global linear resolvent operator. These forcing-response wave packets ("resolvent modes") are first discussed with regard to relevant physical mechanisms that provide energy gain of flow perturbations in the jet. Modal shear instability and the nonmodal Orr mechanism are identified as dominant elements, cleanly separated between the optimal and suboptimal forcing-response pairs. A theoretical development in the framework of spectral covariance dynamics then explicates the link between linear harmonic forcing-response structures and the cross-spectral density (CSD) of stochastic turbulent fluctuations. A low-rank model of the CSD at given Strouhal number is formulated from a truncated set of linear resolvent modes. Corresponding experimental CSD matrices are constructed from extensive two-point velocity measurements. Their eigenmodes (spectral proper orthogonal or SPOD modes) represent coherent wave-packet structures, and these are compared to their counterparts obtained from the linear model. Close agreement is demonstrated in the range of "preferred mode" Strouhal numbers, around a value of 0.4, between the leading coherent wave-packet structures as educed from the experiment and from the linear resolvent-based model.

I. INTRODUCTION

The presence of orderly structures in many turbulent shear flows has been abundantly documented over the past fifty years; in the case of jets, such studies have largely been motivated by the need to reduce their noise generation. It was recognized early on that coherent structures in turbulent jets strongly resemble instability wave packets, as if they were governed by linear dynamics of small-amplitude fluctuations in a time-averaged mean flow [1]. Many variants of linear analysis techniques have since been explored, in order to identify a model that may faithfully reproduce the coherent turbulence structures in jets. Based on the assumption that linear jet instability is driven by incoming disturbances from upstream, Michalke [2] computed the spatial growth of linear perturbations in parallel jet profiles, followed by the inclusion of weakly nonparallel effects by way of multiple-scales expansion [3,4] or parabolized stability equations (PSE [5]), as well as fully nonparallel linear simulations with inlet forcing [6]. As discussed by Jordan and Colonius [1], all these studies successfully predict the observed spatial growth of coherent turbulence structures near the nozzle, over a dominant but restricted range of frequencies. However, the underlying theoretical model *a priori* pertains to deterministic linear perturbations developing in a steady laminar base

flow, and the justification for extending it to chaotic nonlinear fluctuations around a statistical turbulent mean state has remained vague.

Model equations that govern the statistical moments of turbulent flow, like average and co-variance values, can be constructed by considering the linearized Navier-Stokes system subject to stochastic forcing [7]; this approach has recently evolved into the statistical state dynamics frame-work, where stochastic forcing of higher order statistical moments is considered [8]. Application of this framework to the aerodynamic turbulent jet problem is very promising; the interpretation, given on page 6 in Ref. [8], that "turbulence in shear flow can be essentially understood as determined by quasi-linear interaction occurring directly between a spatial or temporal mean flow and perturbations" whereas "the role of nonlinearity in the dynamics of turbulence is highly restricted" is clearly born out by the empirical evidence of turbulent jet studies [1]. While most of the literature on stochastic forcing in the linearized Navier-Stokes equations, including the reviews by Schmid (Sec. 4 in Ref. [9]) and Bagheri *et al.* [10], focuses on time-domain formulations of covariance dynamics, coherence in jet turbulence has often been analyzed in the frequency domain. In particular, several recent jet studies make use of *spectral proper orthogonal decomposition* (SPOD, see Ref. [11], not to be confused with Ref. [12]) as a means to extract empirical coherent structures at a given frequency from experimental or numerical flow data [5,13,14].

Linear instability analysis of jets in recent years has increasingly been carried out in a frequency-domain framework based on *optimal* forcing and associated flow response structures, with no limiting assumptions about the spatial development of the base state [15–21]. Forcing and response structures in this formalism are distributed throughout the interior of the flow, in contrast to the assumption of pure upstream boundary forcing made in most previous models (as cited above), and they are found as the singular modes of the global resolvent operator [9]. This global resolvent framework, also referred to as "frequency response" [15,22] or "input-output" [17] analysis, has similarly been applied in the study of boundary layers [23–25], and its potential for the modeling of stochastic dynamics has been explored for backward-facing step flow [26–28]. The question at this point remains, exactly what stochastic quantities can be consistently modeled on the basis of linear resolvent analysis? Dergham *et al.* [26] use a low-rank resolvent model in order to construct approximations of time-domain POD modes, whereas Boujo and Gallaire [27] follow the arguments of Farrell and Ioannou [22] in order to estimate the frequency spectrum of the stochastic flow response to white-noise forcing. Beneddine *et al.* [28] go further and set out to model the *spatial distribution* of coherent fluctuations in the frequency domain; they demonstrate convincing agreement between the spatial structures of the optimal linear flow response and the leading SPOD mode, obtained from numerical simulations.

A formal justification for a direct comparison between optimal linear response structures and SPOD modes has been suggested by Beneddine *et al.* [28], and, with an increasing level of detail, in two conference papers [19,29] and by Towne *et al.* [20], who also examine the link between resolvent modes and dynamic mode decomposition (DMD). A recent review article [30] provides a didactical introduction to resolvent-based modeling of SPOD modes, including numerical codes for a simple model problem, and a discussion of its relevance for the study of jet noise. Schmidt *et al.* [21] present a detailed comparison between resolvent analysis results and SPOD modes, extracted from LES data, for high-Reynolds-number turbulent jets at Mach numbers 0.4, 0.9, and 1.5. It is found that the leading SPOD mode is well reproduced by the optimal linear flow response, at the dominant Strouhal number 0.6 for the Ma = 0.4 case.

The present paper revisits the same turbulent jet configuration, at Mach number 0.4 and Reynolds number 460 000, entirely based on the experimental measurements by Cavalieri *et al.* [13] and Jaunet *et al.* [31]. The latter study involved velocity measurements in cross-planes of the jet by means of two high-cadence, stereoscopic particle-image velocimetry systems that could be displaced in the streamwise direction so as to provide the cross-spectral density (CSD) of the velocity fluctuations, decomposed both in frequency and in azimuth. In this paper, SPOD modes will be extracted from these experimental CSD matrices, such that they can be compared with linear predictions derived from a resolvent analysis of the experimental mean flow. The principal
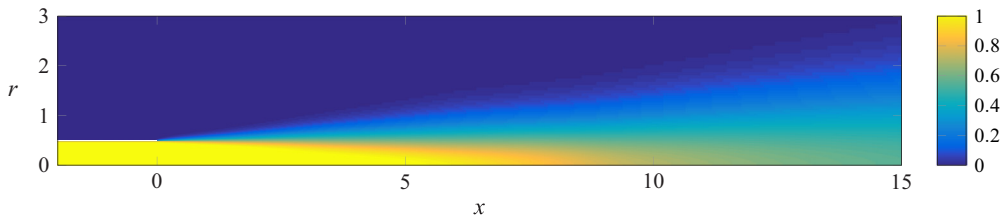
FIG. 1. Axial velocity of the mean flow, as used throughout this study [33]. The distribution has been modeled such as to closely reproduce the experimental measurements [13]. The pipe wall is represented as a white line, and only a portion of the numerical domain is shown. The rasterization of the color plot corresponds to the standard numerical grid resolution (Sec. III D).

new aspects of the present study are (i) the use of an experimental database for jet resolvent analysis, (ii) the extraction of SPOD modes from experimental jet measurements, (iii) the design of a *resolvent-based linear model* for such experimental SPOD modes, which are necessarily based on partial-state information, and (iv) a detailed discussion of the linear instability dynamics triggered by optimal and suboptimal forcing in thin-shear-layer jets, which, by extension, underpin the spectral covariance dynamics contained in the SPOD modes. Although the results of this study are mostly consistent with those of Schmidt *et al.* [21], several quantitative as well as qualitative differences arise, with relevance for the physical interpretation in terms of instability mechanisms. These differences are attributed to the inclusion of a nozzle pipe in the present analysis. The nozzle boundary layer is identified as the most receptive flow region in the following calculations, underlining the importance of its numerical resolution, similar to recent observations in large-eddy simulations (LES) [32].

The flow configuration, corresponding to the jet experiments, is briefly defined in Sec. II. The linear resolvent analysis, including the modal decomposition framework, the numerical implementation, and the presentation of results, is documented in Sec. III. This is followed, in Sec. IV, by a discussion of the salient linear instability mechanisms that are active in optimal and suboptimal jet forcing. Section V presents a detailed comparison between SPOD modes from experimental data and stochastic predictions derived from the resolvent-based linear model. Our new results are then put into perspective with regard to previous modeling attempts. The paper closes, in Sec. VI, with a summary of the main conclusions.

II. FLOW CONFIGURATION

The study is based on jet experiments conducted at the Bruit et Vent jet-noise facility of the Pprime Institute in Poitiers. Technical details of the experimental apparatus, as well as measurement validation, are thoroughly described in past publications [13,31].

The experiments are performed on a $Ma = 0.4$ isothermal jet issuing from a convergent-straight nozzle. The Reynolds number of the jet, based on the nozzle exit diameter $D = 50$ mm and the maximum exit velocity U_j, is defined as $Re = U_j D/\nu = 460\,000$, where ν is the kinematic viscosity. The Strouhal number corresponding to the dimensional frequency f is defined as $St = fD/U_j$. The transition to turbulence of the incoming boundary layer is forced using an azimuthally homogeneous carborandum strip, such that a fully turbulent boundary layer is obtained at the exit section of the nozzle (see Fig. 1 in Ref. [13]).

Free-jet mean flow measurements from this setup, obtained with a Pitot tube, are available from the experiments by Cavalieri *et al.* [13], and excellent reproducibility has been demonstrated in the more recent experiments by Jaunet *et al.* [31]. These experimental data are used to construct a parametric model of the mean flow, providing smooth variations of axial and radial velocity, density, and temperature [33]. The modeled axial velocity field is shown in Fig. 1. In the free-jet region, our modeling procedure follows closely the one described in Rodriguez *et al.* [14], but the
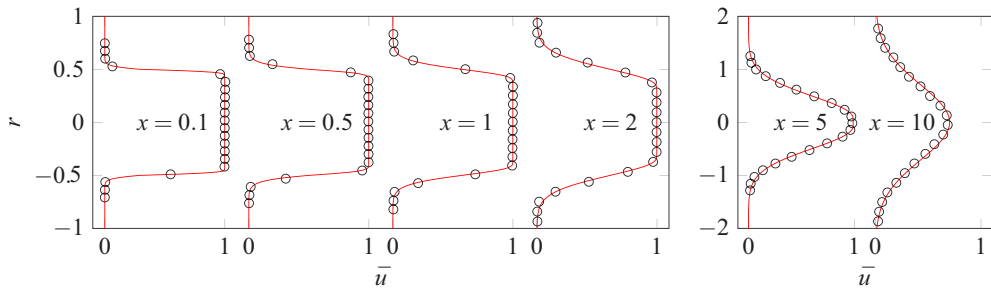
FIG. 2. Comparison of axial velocity profiles along r, at various x locations, between the numerically modeled mean flow (red lines) and the experimental measurements [13] (circles).

present mean flow in our numerical domain has been entirely computed anew from the experimental reference data. It includes a straight pipe that is added upstream of the nozzle exit $x = 0$, and the mean flow inside this pipe is taken to be parallel. Twenty-one experimental velocity profiles in the free jet are available between $x = 0.1D$ and $x = 10D$; some of these are compared in Fig. 2 to the modeled mean flow at selected x locations. At $x = 6.2D$, the interpolated center line velocity falls below $0.95 U_j$, which may be taken to mark the end of the potential core. Downstream of $x = 10D$, a self-similar development is assumed, according to the solution discussed in Sec. 5.2 of Ref. [34],

$$\bar{u}(r, x) = \frac{\bar{u}(0, x)}{(1 + c_1 \eta^2)^2} \quad \text{with } \eta = \frac{r}{x - x_0} \text{ and } \bar{u}(0, x) = \frac{c_2}{x - x_0}. \tag{1}$$

The parameters c_1 and c_2, as well as the virtual origin x_0, are determined from the available experimental profiles. Parallel nozzle flow, near-nozzle jet, and self-similar far field constitute three distinct flow regions, and smooth transitions between these three are enforced by means of weighted superposition in overlap zones [15,35]. Residual nonsmoothness in the derivatives of the reconstructed mean flow is removed by applying high-order explicit filtering. The final axial velocity field (Fig. 1) is used for computing temperature and density distributions by way of the Crocco-Busemann relation, and the radial velocity component is recovered from the continuity equation [14].

The momentum thickness of the free-jet shear layer, defined at a given x position as

$$\delta_m = \int_0^{r_{\max}} \frac{\bar{\rho}\bar{u}}{\rho_\infty U_j}\left(1 - \frac{\bar{u}}{U_j}\right) dr, \tag{2}$$

grows linearly in x, at a rate of $d\delta_m/dx \approx 0.031$. This variation is extrapolated upstream from $x = 0.1D$ to the nozzle exit at $x = 0$, resulting in a momentum thickness $\delta_m(x = 0) = 0.0075D$, significantly thinner than in the LES-based study by Schmidt *et al.* [Ref. [21], their Fig. 2(b)]. This exit profile is taken between $0 \leqslant r \leqslant D/2$ to form the parallel flow inside the nozzle, with a linear decay to zero over the first few discretisation points nearest the wall interior. This parallel flow has a thickness $\delta_m = 0.0055D$, when evaluated according to (2) with $r_{\max} = D/2$.

III. LINEAR RESOLVENT ANALYSIS OF FLUCTUATIONS AROUND A MEAN FLOW

A. Governing equations

We consider the compressible Navier-Stokes equations, in terms of conservative variables $(\rho, \rho\mathbf{u}, \rho E)$, cast in axisymmetric cylindrical coordinates (x, r). In the notation of Ref. [36], these

equations are

$$\frac{\partial \rho}{\partial t} + \nabla(\rho \mathbf{u}) = 0, \tag{3a}$$

$$\frac{\partial \rho \mathbf{u}}{\partial t} + \nabla(\rho \mathbf{u} \otimes \mathbf{u}) = -\nabla p + \nabla \tau, \tag{3b}$$

$$\frac{\partial \rho E}{\partial t} + \nabla(\rho \mathbf{u} E) = -\nabla \mathbf{h} + \nabla(\tau \mathbf{u}), \tag{3c}$$

where ρ is density and $\mathbf{u} = (u_x, u_r, 0)$ is the velocity vector, with axial and radial components u_x and u_r, and with zero azimuthal velocity. In our axisymmetric setting, all quantities are independent of the azimuthal coordinate θ. The total energy E is then defined as

$$E = \frac{T}{\gamma(\gamma - 1)Ma^2} + \frac{1}{2}(|u_x|^2 + |u_r|^2), \tag{4}$$

with $\gamma = 1.4$ being the ratio of specific heats. The tensor τ denotes the molecular stresses, and $\mathbf{h}$ is the heat flux vector. The reference length of the problem is the pipe diameter D. The reference velocity is chosen as the center-line velocity U_j at the pipe exit $x = 0$, and the reference density is set as the ambient value ρ_∞. Sutherland's law is used to calculate the viscosity, and the Prandtl number is set to $\mathrm{Pr} = 0.72$, the standard value for air.

B. Representation as a linear input-output system

The flow variables $q = (\rho, \rho u_x, \rho u_r, \rho E)$ are decomposed into their time-averaged mean and time-dependent fluctuation components, $q(x, r, t) = \bar{q}(x, r) + q'(x, r, t)$. The governing equations (3) can then be rewritten in the form

$$\frac{\partial q'}{\partial t} - Aq' = f, \tag{5}$$

where A is the operator obtained by linearizing (3) around the mean flow, and the vector f contains all remaining nonlinearities in q', i.e., the fluctuations of the generalised Reynolds stresses [37], as well as any external forcing at the boundaries of a finite-domain flow problem. The vector f thus contains zero-mean source terms of the continuity, momentum, and energy equations.

A Fourier-transform

$$q'(x, r, t) = \int_{-\infty}^{\infty} \hat{q}(x, r, \omega)e^{i\omega t} d\omega, \quad f(x, r, t) = \int_{-\infty}^{\infty} \hat{f}(x, r, \omega)e^{i\omega t} d\omega, \tag{6}$$

leads to the frequency-domain system

$$\hat{q} = (i\omega I - A)^{-1}\hat{f} = R(\omega)\hat{f}, \tag{7}$$

where R is the *resolvent* operator [9]. As f contains all terms nonlinear in q', the forcing with its Fourier-transform $\hat{f}$ induces an inherent coupling between all frequencies. In order to make use of the system (7) for the purpose of modeling, a closure assumption is required that allows a decoupling of frequencies. Following previous literature [20,22,28,38], we choose to simply regard f as an anonymous forcing term, representing any incoming perturbations from the nozzle or the ambient, as well as fluctuations in the nonlinear terms of the momentum and energy equations, but without accounting for its inner structure that makes it dependent on q'. Accordingly, we neglect the dependence of $\hat{f}$ at one given frequency on $\hat{q}$ at other frequencies.

One possibility to account for a limited interaction between frequencies lies in the inclusion of turbulent dissipation through small scales in the linear operator A, in the form of turbulent viscosity. Indeed, any portion of $\hat{f}$ may be modeled as being linearly dependent on $\hat{q}$, without introducing explicit coupling between frequencies. Some empirical evidence suggests the pertinence of such modeling [39,40], and we have used it in the past for the resolvent analysis of turbulent jets [18,41],

but the procedure requires additional modeling hypotheses and is not pursued here. All computations in this section only account for molecular viscosity at Re $= 460\,000$.

C. Modal decomposition of the resolvent operator

First attempts to model the global linear response of shear flows to forcing were based on eigenmode decomposition, e.g., Ref. [42]. However, it has generally been realized that *amplifier-type* flow dynamics [43] are not adequately described by their spectrum of stable eigenmodes. For jet flows, this case is made by Garnaud *et al.* [44]. Instead, a decomposition approach based on *singular modes* (SVD) is conceptually well suited.

The following development restates the SVD-based resolvent analysis formalism as it has been applied in numerous past studies, including Refs. [15,17–21]. It is presented here in a form that establishes our nomenclature and clarifies the influence of the chosen energy norm.

For a given frequency ω, the resolvent operator provides the mapping between any forcing structure $\hat{f}(x, r, \omega)$ and its linear flow response $\hat{q}(x, r, \omega)$. The common choice for an energy measure in compressible settings is the norm defined by Chu [45],

$$\|\hat{q}\|^2 = \iint_\Omega \left[\bar{\rho}(|u_x|^2 + |u_r|^2) + \frac{\bar{p}}{\bar{\rho}}|\hat{\rho}|^2 + \frac{\bar{\rho}^2}{\gamma^2(\gamma - 1)Ma^4\bar{p}}|\hat{T}|^2 \right] r\, dr\, dx, \quad (8)$$

which is used in the following computations. Both the forcing and the flow response are measured in this norm, and the spatial integration in both cases is carried out over the entire numerical domain Ω, with the exception of absorbing layers near the outer boundaries (see Sec. III D). In discrete form, the norm is expressed by a Hermitian positive-definite matrix M, such that $\|\hat{q}\|^2 = \hat{q}^H M \hat{q}$, with a Cholesky factorization $M = N^H N$. Flow forcing and response are represented by *discrete* complex-valued vectors $\hat{f}$ and $\hat{q}$ in the following.

The *gain* between input and output energy is then defined as

$$\sigma^2 = \frac{\|\hat{q}\|^2}{\|\hat{f}\|^2} = \frac{\hat{f}^H R^H M R \hat{f}}{\hat{f}^H M \hat{f}} = \frac{\hat{v}^H N^{-1,H} R^H M R N^{-1} \hat{v}}{\hat{v}^H \hat{v}}, \quad \text{with } \hat{v} = N\hat{f}, \quad (9)$$

which has the form of a Rayleigh quotient, involving the Hermitian operator $N^{-1,H} R^H M R N^{-1}$. Consequently, the eigenvectors $\hat{v}_i$ of this operator are orthogonal, its eigenvalues σ_i^2 are real positive, and the largest possible energy gain of the linear flow system is given by the largest eigenvalue. The forcing structure that gives rise to an energy gain σ_i^2 is recovered as $\hat{f}_i = N^{-1}\hat{v}_i$. After normalization, $\hat{v}_i^H \hat{v}_i = 1$, the eigenvectors $\hat{v}_i$ are the columns of the right singular matrix V of the operator

$$NRN^{-1} = U\Sigma V^H, \quad (10)$$

associated with the singular values σ_i as entries in the diagonal matrix Σ, and with the unique unitary matrix U.

The forcing structures $\hat{f}_i$ are the columns of a matrix $F = N^{-1}V$, and the associated flow response structures $\hat{q}_i$ form the matrix $\hat{Q} = RF$. With (10), it is found that $\hat{Q} = N^{-1}U\Sigma$, from where it follows that $\hat{Q}^H M \hat{Q} = \Sigma^2$. A normalized response matrix $Q = \hat{Q}\Sigma^{-1}$ is introduced, such that the final identities for our modal resolvent decomposition are recovered:

$$F^H M F = Q^H M Q = I, \quad (11a)$$

$$R = Q\Sigma F^H M. \quad (11b)$$

The singular values σ_i are arranged in descending order, such that the optimal energy gain is given by $\sigma_{\max}^2 = \sigma_1^2$, arising for the forcing structure $\hat{f}_1$. In the inner-product space defined with the matrix M, each vector $\hat{f}_j$ represents the optimal forcing in the subspace that is orthogonal to all leading vectors $\hat{f}_i$ with $i > j$. As a convention, we will refer to a given triple $(\sigma_i, \hat{f}_i, \hat{q}_i)$ as the resolvent mode i, consisting of the ith gain, forcing mode, and response mode. The triple $(\sigma_1, \hat{f}_1, \hat{q}_1)$
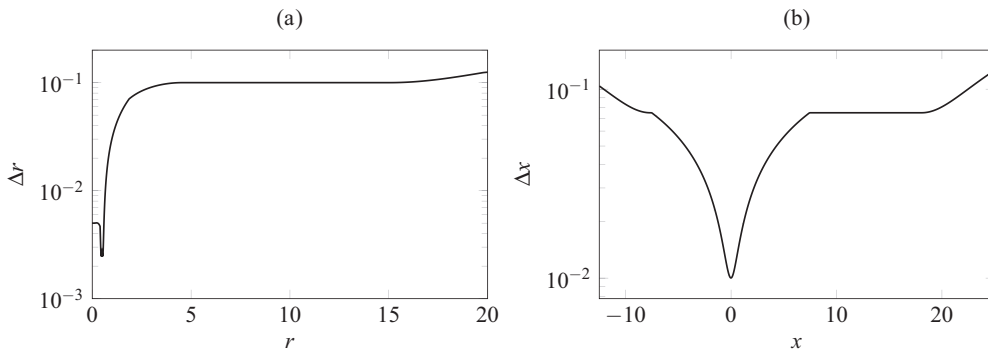
FIG. 3. Spacing of mesh points (a) in the radial direction and (b) in the axial direction. The mesh is orthogonal.

of optimal gain, optimal forcing, and optimal response is characterized by the maximum value of σ, and resolvent modes with $i > 1$ are sometimes referred to as suboptimals. Note that gain in the following refers to σ, not to the *energy* gain, given by σ^2.

D. Matrix-free computation of resolvent modes

Gain values and associated forcing modes are computed by solving the reformulated eigenvalue problem

$$R^H M R \hat{f}_i = \sigma_i^2 M \hat{f}_i, \tag{12}$$

using the iterative Lanczos method that is provided by the SLEPc library [46]. A matrix-free time-stepping method is used in each iteration step, as described in detail in Ref. [35]. Time stepping needs to be performed both for the solution of a direct system, $a = Rb$, and for the subsequent solution of an adjoint system, $a' = R^H b'$. The time horizon t_{max} of these calculations must be chosen long enough such that the final periodic flow regime is recovered with sufficient accuracy. A numerical procedure for the adjoint system is constructed according to the method of Fosas de Pando *et al.* [47], which ensures that the complete numerical encoding of the operator in (12) remains strictly Hermitian; this is an important requirement for the efficiency of the Lanczos algorithm.

The linear system (5) is discretized with explicit finite-difference schemes [48], using an 11-point stencil. Time integration is performed with a third-order Runge-Kutta algorithm, with time step $\Delta t = 2.85 \times 10^{-3}$. The computational domain extends along the streamwise direction over the interval $x \in [-12.5, 25]$, and from the symmetry axis $r = 0$ outward to $r = 20$; the nozzle exit is placed at $x = 0$. The mesh that is used in all calculations presented in the following sections consists of $(N_x, N_r) = (750, 380)$ discretization points. These points are distributed on a nonuniform Cartesian grid, with maximum resolution along the pipe walls, in the shear layer and around the nozzle lip. Figure 3 displays the axial and radial point distributions.

Symmetry boundary conditions are imposed on the jet axis by the use of ghost points: ρ, ρu_x, and ρE are prescribed to be even functions in r across the axis, while ρu_r is odd. On all other boundaries, the LODI boundary conditions are applied [49], in combination with absorbing layers [50] at $r > 16$, $x < -8$, and $x > 21$.

Convergence of the optimal gain is tested with respect to the grid spacing and to the final time t_{max} of the simulations. Several results are reported in Table I. For a fixed value $t_{max} = 60$, the mesh of case C0 is deemed sufficiently refined; this is the standard mesh displayed in Fig. 3. The final time is chosen by tracking the energy of time-harmonic fluctuations, in order to evaluate to what extent transient dynamics have died out. Satisfactory convergence is reached at $t_{max} = 80$, which corresponds approximately to twice the convection time of vortical structures between the

TABLE I. Convergence of the optimal gain σ_1 at St = 0.5, as a function of grid resolution and final simulation time t_{max}. These test calculations were performed with a reduced Krylov space dimension $N_{kr} = 4$. A value of $N_{kr} = 12$ is used in all following computations for increased accuracy of suboptimal modes.

	Δx_{min}	Δr_{min}	t_{max}	σ_1
Case A	0.0200	0.0075	60	5117.2
Case B	0.0200	0.0025	60	5256.3
Case C0	0.0100	0.0025	60	5264.3
Case C1	0.0100	0.0025	70	5294.4
Case C2	0.0100	0.0025	75	5302.6
Case C3	0.0100	0.0025	80	5306.6

nozzle exit and the downstream end of the physical domain; this value is retained for all following calculations.

For any given Strouhal number, the five leading resolvent modes are computed, using a Krylov space of dimension $N_{kr} = 12$. The Lanczos iteration is halted when the estimated residual norms of all five modes have fallen below the tolerance value $\epsilon = 10^{-4}$ (see Ref. [46]), implying confidence in the first four significant digits of the gain values. A typical computation for one Strouhal number requires about 12–16 wall-time hours on 192 cores of Intel Xeon E5-2690 v3 CPUs.

E. Resolvent mode results

Gain values of the five leading resolvent modes are shown in Fig. 4 as functions of the Strouhal number. Above St = 0.3, the optimal gain curve is well separated from the suboptimal ones. The maximum overall gain occurs at St = 0.7, where σ_1 is one order of magnitude larger than σ_2.

The optimal forcing and response structures are presented in Figs. 5 and 6 for several Strouhal numbers between 0.2 and 0.7; snapshots of the real axial momentum components are shown in all frames, with a rasterization that corresponds to the numerical mesh. At Strouhal numbers 0.3 and above, the forcing is localized in a thin layer at the inner pipe wall, near the nozzle. The right-column frames in Fig. 5 give a magnified view of the forcing in this flow region. Elongated structures are tilted against the flow direction, in a fashion that is typical of the Orr mechanism (see Sec. IV for a brief description of this phenomenon). Similar optimal forcing structures
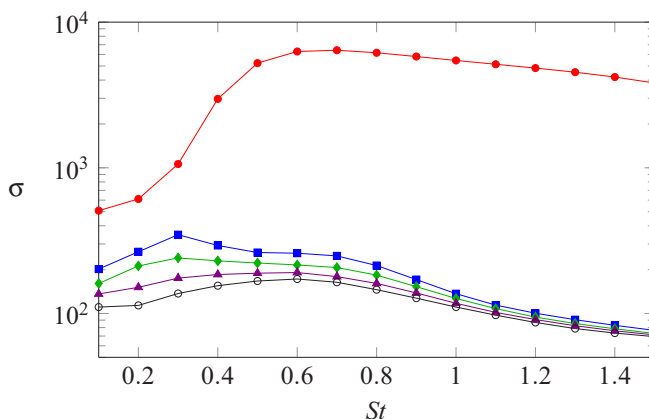

FIG. 4. The five leading resolvent gain values (● σ_1, ■ σ_2, ◆ σ_3, ▲ σ_4, ○ σ_5) as functions of Strouhal number.
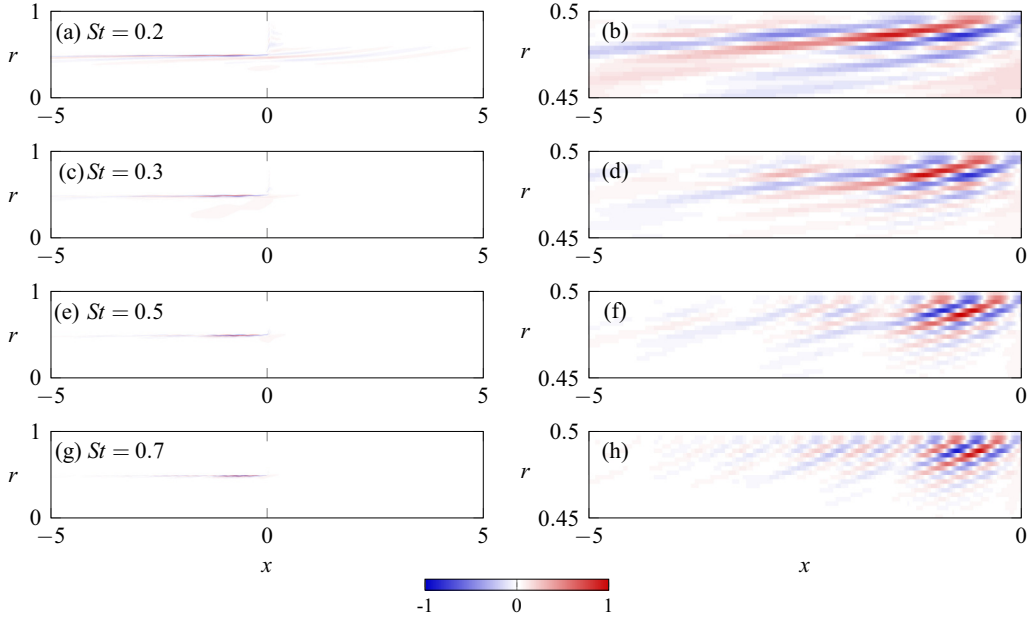
FIG. 5. Optimal forcing modes at various Strouhal numbers, associated with the response modes in Fig. 6. The real part of axial velocity forcing is represented. [(a), (c), (e), (g)] Optimal forcing, plotted with aspect ratio 2. [(b), (d), (f), (h)] Closeup of the pipe boundary layer, where the forcing is localized, at the same St values as in the left column. The rasterization corresponds to the numerical mesh; each field is normalized with respect to its maximum amplitude.

have been identified in boundary layers [23,24] and in past studies of incompressible as well as compressible jets [15,16,18]. The response structures at St $\geqslant$ 0.3 exhibit the classical wave-packet shape associated with shear instability, with peak amplitudes inside the potential core [14,15,21].

The main characteristics of both the optimal forcing and the optimal response modes are similar at all Strouhal numbers above 0.2: Optimal forcing acts upstream in the pipe and generates a wave packet with amplitude growth in the potential core region of the jet. As the Strouhal number
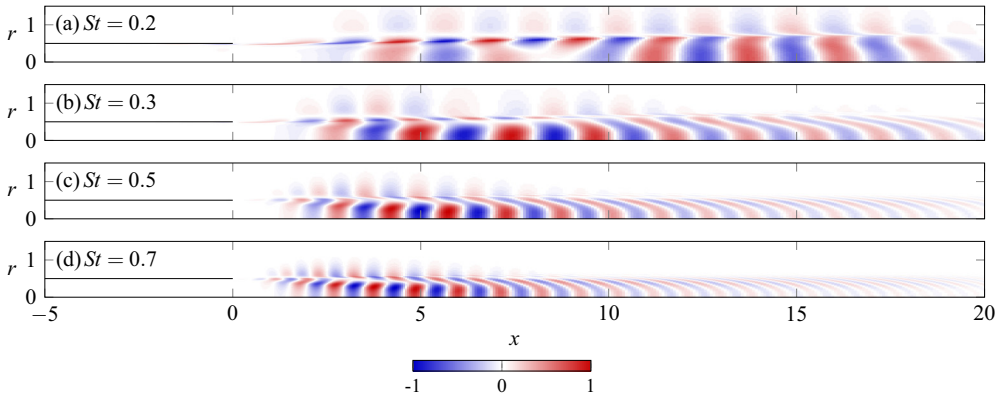

FIG. 6. Optimal response modes at various Strouhal numbers, associated with the forcing modes in Fig. 5. The real part of axial velocity perturbations is represented, with aspect ratio 1. The pipe wall is shown as a black line. Each field is normalized with respect to its maximum amplitude.
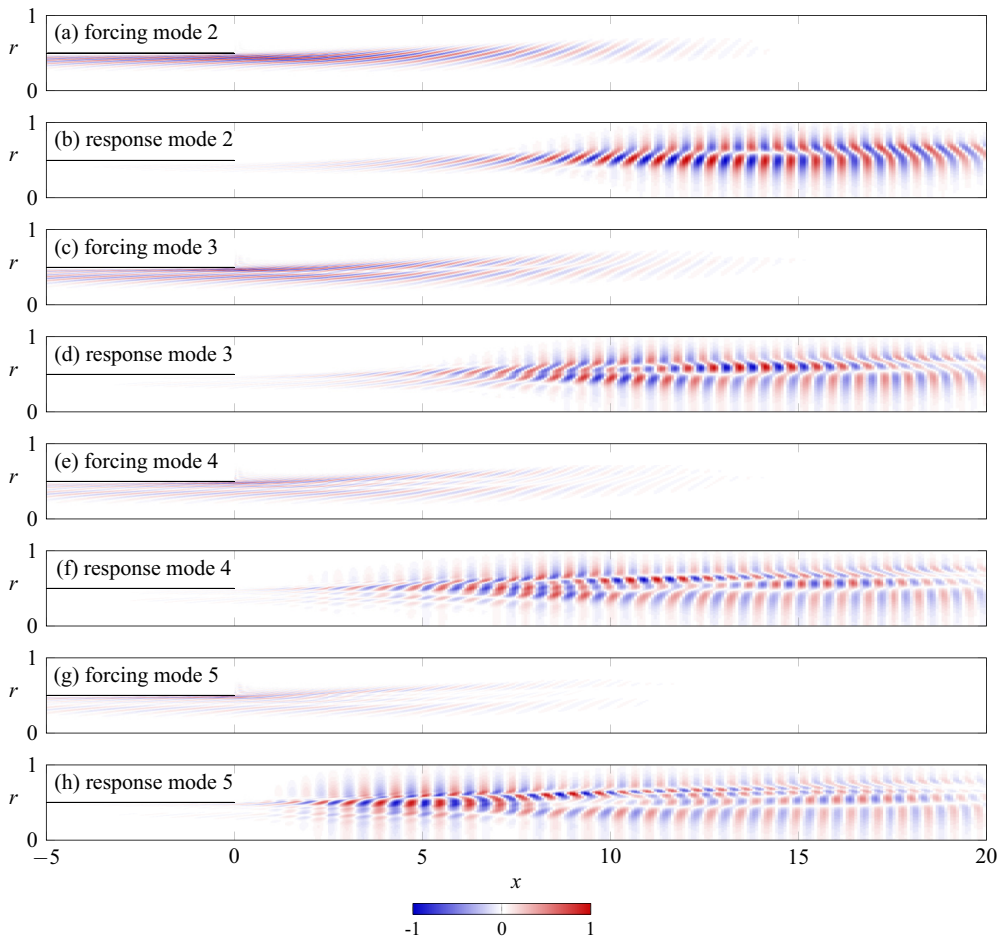
FIG. 7. Suboptimal forcing and response modes for St = 0.7. The real part of axial velocity perturbations is represented. [(a), (c), (e), (g)] Forcing modes and [(b), (d), (f), (h)] associated response modes. The pipe wall is shown as a black line. Each field is normalized with respect to its maximum amplitude. The aspect ratio is 2, and strong magnification is required in order to visualize the fine-scale radial variations.

increases, the wavelength shortens, and the location of the peak amplitude moves closer to the nozzle, consistent with the interpretation of local spatial instability [2]. At low Strouhal numbers, as shown in Figs. 5(a) and 6(a), different effects seem to arise: In addition to the described scenario, tilted forcing structures protrude into the free shear layer close to the nozzle, and the response wave packet appears to be composed of two distinct regions. Along the jet axis, one local amplitude maximum occurs at $x = 5.5$, and another one at $x = 13$, far downstream of the potential core. The low-St optimal mode results of Schmidt *et al.* (Fig. 12(f) in Ref. [21]) show a similar pattern. As argued by those authors, the distinct mode characteristics at low Strouhal numbers are likely to be associated with a crossing or merging of mode branches, due to a lessened efficiency of the shear instability mechanism.

Suboptimal forcing and response structures, modes 2–5, are displayed in Fig. 7 for St = 0.7. The forcing in all cases is again characterized by structures that are tilted against the mean flow, although these structures arise at a small radial distance away from the pipe wall, and they extend far into the free jet, with significant amplitude inside the shear region. The associated response wave packets have their maximum amplitude far downstream of the potential core. The forcing structures

display radial variations that are suggestive of orthogonal functions, with an increasing number of zero-amplitude nodes along r, and corresponding radial structures are imparted to the response wave packets. A similar hierarchy of optimal modes has been described in Ref. [18].

Preliminary results, pertaining to the same flow configuration of the jet experiments, have been presented in a previous conference paper [19]. While all forcing modes in that paper are visually identical to the present results, the associated suboptimal response modes were quite different, all bearing a strong resemblance to the optimal mode. Those earlier calculations were clearly affected by spurious numerical noise, which in all cases triggered the optimal mode sufficiently so as to overwhelm the true suboptimal response. Nonsmoothness in the base flow, as used in Ref. [19], was identified as the cause of this spurious effect. It has been carefully verified that forcing and response modes in the present results form orthogonal sets, with respect to our scalar product, within the accuracy imposed by the residual tolerance of the Lanczos algorithm.

IV. INTERPRETATION OF OPTIMAL GROWTH MECHANISMS

The role of modal shear (Kelvin-Helmholtz) and nonmodal Orr mechanisms for optimal and suboptimal jet resolvent modes has often been invoked in the literature (see, for instance, Refs. [21,51,52]). The aim of this section is to substantiate this interpretation by use of local analysis (for shear) and a parallel model flow (for Orr).

The Orr mechanism denotes a linear phenomenon of vorticity convection in a sheared mean flow that gives rise to a growth of perturbation energy. Vortical perturbation structures of alternating sign, initially tilted at an angle opposite to the mean shear, are convected by the mean flow in a way that their tilting angle is first reduced, until the vortex structures are aligned perpendicular to the main flow direction. This deformation is accompanied by an algebraic energy growth of the perturbations. Subsequently, the structures are tilted further, such that they are increasingly aligned with the main flow direction; this phase is accompanied by energy decay. An example of the Orr scenario in a parallel jet is discussed in the second half of this section. Butler and Farrell [53] investigate the mechanisms of energy transfer between perturbations and the mean flow for this phenomenon, based on the Reynolds-Orr equation, in the context of an initial perturbation that evolves in time. They interpret the energy growth as being caused by an interaction of mean shear and perturbation Reynolds stresses, whereas Jiménez [54] describes it as being the result of mass conservation.

Our optimal resolvent modes (Fig. 6) strongly resemble those described by Garnaud *et al.* [15] for an incompressible turbulent jet, which have been interpreted as a constructive combination of the Orr mechanism in the pipe boundary layer and the shear mechanism in the free jet. Close to the nozzle, the optimal response modes display peak amplitudes inside the free shear layer, when measured along the radial direction. As discussed in Ref. [15], and consistent with many other studies on jet wave packets (e.g., Refs. [14,21]), the spatial distribution as well as the strong streamwise amplitude growth indicates a preponderant role of shear instability in the optimal forcing response. This hypothesis is easily validated by a comparison with local instability results in the near-nozzle region. In a local framework, the shear instability mechanism gives rise to a single spatial k^+ mode, which is indeed the only unstable spatial mode that can be found in the jet [55]. The downstream evolution of this k^+ eigenvalue, for $St = 0.7$ in the present jet mean flow, is displayed in Fig. 8 in terms of its spatial growth rate $-k_i$ and its real phase velocity $c_r = -\omega/k$. The latter is further scaled with the *local* centerline velocity $U_c(x)$ of the jet profile.

The local shear instability mode, for $St = 0.7$, is seen to be unstable only over the interval $0 \leqslant x \leqslant 2.17$. Downstream of this position, its eigenfunction (not shown) develops strong oscillations around $r = 0.5$, characteristic of the viscous solution in the Stokes sector above the critical point [56], and it remains numerically tractable with confidence over only a short distance further. A Reynolds number of 20 000 has been used in these local calculations, lower than in the reference experiment and in the global resolvent analysis, in order to accommodate an accurate resolution of eigenfunctions in the slightly stable regime. It can be demonstrated that results in the *unstable*
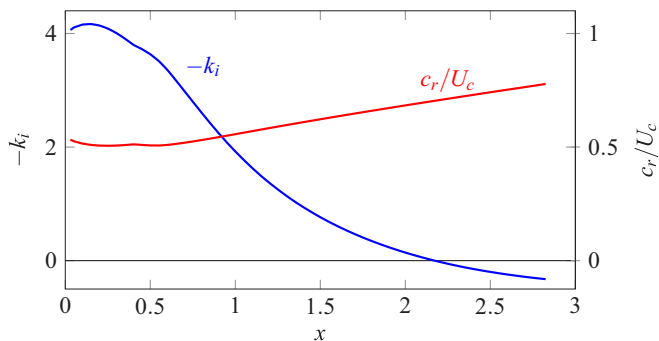
FIG. 8. Growth rate $-k_i$ and real phase velocity c_r of the local shear instability mode, and their downstream variations in the jet mean flow. The phase velocity is scaled with the local mean centerline velocity.

regime are unaffected by this large value of Re. Relevant details on local spectra of compressible jets are discussed by Rodriguez *et al.* [14]; in particular, it is described how the shear layer mode, once it is stable, quickly merges into a continuous branch of oscillating modes. The same observations apply here.

Following the method of Rodriguez *et al.* [14], the optimal resolvent response wave packet at St = 0.7 [Fig. 9(a)] is projected at each x onto the complete basis of local spatial eigenfunctions, by an inner product with the associated local adjoint modes. Projection coefficients are thus obtained at each x position, and the superposition of all local modes indeed fully reproduces the entire global response wave packet. The isolated contribution of the local k^+ shear mode is shown in Fig. 9(b) over the streamwise region where this mode is identifiable without ambiguity. It is seen that this mode alone accounts rather accurately for the optimal resolvent response in the unstable interval $0 \leqslant x \leqslant 2.17$. Downstream of this region, the radial distribution of the local eigenfunction differs notably from the global result and, contrary to the discussion in Ref. [15], no other single local mode can be identified as being dominant anywhere for $x > 2.17$. The global structure in that region projects significantly onto a large number of local modes from a continuous branch, with strong nonorthogonal cancellation effects.

The second resolvent response structure (mode 2) at St = 0.7 [Fig. 7(b)] cannot be related to any dominant local mode anywhere along x. As perturbation growth in the resolvent mode is observed down to a streamwise station $x = 14$, it is already obvious that this behavior is not attributable to modal growth in a local sense, since local instability at this Strouhal number is confined to $x < 2.17$. Instead, the spatial features of the response wave packet suggest again an action of the Orr
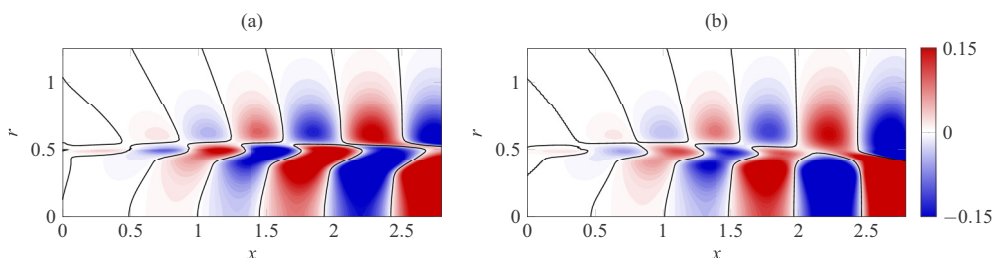

FIG. 9. Local shear instability contribution to the optimal response mode at St = 0.7. (a) Optimal response mode from global resolvent analysis; (b) its reconstruction from projection onto the k^+ local shear instability mode. Axial velocity fluctuations are shown over the interval in x where the local mode can be identified numerically. Both fields are normalized with respect to their amplitude maxima, but the color scale is saturated in order to make small-amplitude fluctuations visible. The zero contour is traced in black.
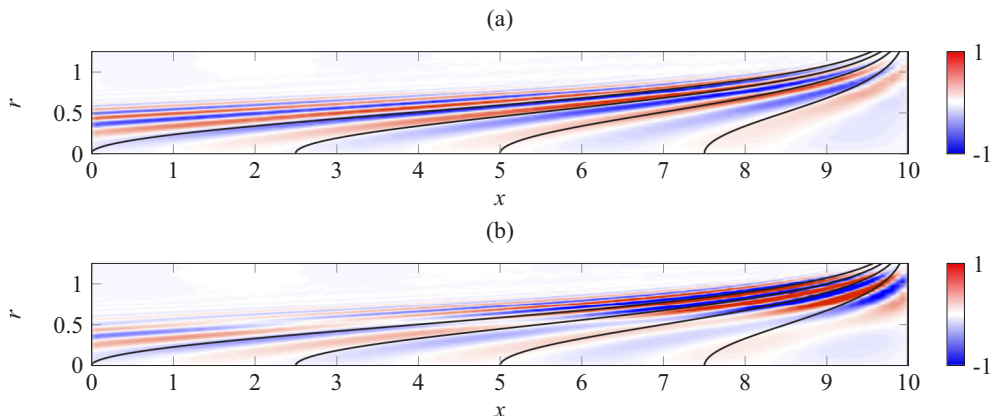
FIG. 10. Forcing mode structures in a parallel incompressible jet with Gaussian base flow profile. Kinetic energy at $x = 10$ is maximized. Streamwise velocity forcing is shown in linear color scale. Black lines: contours that are convected into vertical lines at $x = 10$ after $\Delta t = (2.5, 5, 7.5, 10)$. (a) Forcing mode 1; (b) forcing mode 2.

mechanism, both inside the pipe and in the jet, which feeds on energy gain from the pure convection of tilted vortical structures in a sheared base flow. Such tilted structures are generated by distributed forcing in the free shear layer [Fig. 7(a)] upstream of the response maximum. This mechanism has been described by Tissot *et al.* [51] in a different framework, where PSE and its adjoint are used to determine forcing terms that optimally match experimental results for the same jet as analyzed here. A discussion in terms of local instability modes is not helpful in this case, but the suboptimal forcing mechanism can still be characterized in the setting of a *parallel* jet flow, which will serve as a model problem in order to understand the trends obtained in the nonparallel framework.

A parallel incompressible jet is considered, defined by a Gaussian velocity profile

$$U(r) = e^{-2r^2}, \tag{13}$$

as a simple analytical model for the flow downstream of the potential core. The inflection point is located at $r = 0.5$, and the flow is locally stable at a Reynolds number Re $= 20\,000$. Axisymmetric linear perturbations are computed in a numerical domain of 10 diameters in the axial and radial directions, in response to forcing of both velocity components, which may act anywhere in the domain. The numerical method of Ref. [57] is adapted for the *global* computation of optimal resolvent structures, such that the kinetic energy of the flow response at $x = 10$, integrated in r, is maximized. Thus, forcing is allowed to act throughout the flow domain, but the optimization objective is measured only at the downstream end.

The first two forcing modes are shown in Fig. 10, for a Strouhal number St $= 1/\pi$. Tilted structures are observed, quite similar to the compressible results displayed in Figs. 7(a) and 7(c), and the tilting angle increases with upstream distance from the target position $x = 10$. Black curves trace material lines in the flow that are transported, through convection with the local flow velocity, into vertical lines at $x = 10$ after various time lapses. It is immediately seen that the forcing structures follow closely the local curvature of these contours, especially at far upstream positions. Along the black curves, the phase of the first forcing mode structure is approximately constant, whereas the second mode displays a sign change in the phase at the inflection point $r = 0.5$. This radial sign change provides for the orthogonality between different forcing modes, and their associated flow responses, while the streamwise variations in modes 1 and 2 are nearly identical. The third and fourth forcing modes of the parallel incompressible jet, not shown in Fig. 10, are merely characterized by additional phase changes in the radial direction. All these features are fully

consistent with the suboptimal forcing structures found for the nonparallel compressible jet (Fig. 7). The parallel jet results clearly demonstrate that an Orr-type convection mechanism is responsible for the forcing gain in this locally stable setting. From their resemblance, it is inferred that the same mechanism accounts for the gain of suboptimal structures in the nonparallel compressible jet.

In summary, the following main interpretations of the findings in Sec. III E are proposed: (i) The optimal forcing (mode 1) targets the shear instability of the jet, leading to exponential amplitude growth along x in a finite region directly downstream of the nozzle. Forcing of this mechanism is most efficient at the upstream end of the locally unstable region. Even more efficient than direct forcing of shear-instability perturbations at the nozzle lip is the forcing of Orr structures in the inner pipe boundary layer, which experience growth before they enter the free jet (consistent with Refs. [15,16,18]). (ii) Suboptimal forcing exploits the Orr mechanism in the free jet as a means of perturbation energy growth, independent of modal shear instability. Successive suboptimal modes exhibit an increasing number of sign changes in the phase along r, which accounts for their mutual orthogonality. (iii) In our present results (Sec. III E), the above two mechanisms appear to be well separated in the optimal and suboptimal resolvent modes at moderate Strouhal numbers. At St = 0.2, the shape of the optimal mode [Figs. 5(a) and 6(a)] suggests a mixed excitation of shear instability and free-jet Orr mechanism.

V. COHERENT STRUCTURES IN JET TURBULENCE: EXPERIMENT AND LINEAR MODEL

The resolvent analysis of Sec. III so far only describes the linear flow response to harmonic forcing input. In this section, those results will be leveraged for the modeling of coherent turbulent structures, where both the forcing f and the response q' are of a stochastic nature.

A. Extraction of SPOD modes from experimental data

The jet experiments of Jaunet *et al.* [31] provide an extensive database of synchronous PIV measurements in cross-planes at several axial positions. Two-point coherence statistics along fixed radial positions have been discussed in the first publication [31] with a focus on the streamwise coherence length; here, the same database is fully exploited for the computation of the two-dimensional cross-spectral density of axisymmetric velocity fluctuations in the (x, r) plane. To our knowledge, no experimental CSD measurements of comparable size and detail in a turbulent jet exist in the literature.

The acquisition apparatus consists of two time-resolved stereo-PIV systems that can be moved independently. Both systems measure the velocity in planes orthogonal to the jet axis at either the same axial location (coplanar configuration) or at different positions. A sketch of the setup is shown in Fig. 11(a), where it is illustrated how the two PIV systems can be positioned with respect to the nozzle. The axial positions of the measurement planes are $x_1 \in [1, 8]$ and $x_2 \in [x_1, 8]$ in increments of $\Delta x = 0.5$, where x_1 refers to the axial position of the upstream system (S_1) and x_2 to that of the downstream system (S_2). The instantaneous velocity fields are interpolated onto a polar grid of 32 points in the radial direction and 64 in azimuth, for $r \leqslant 0.8$, using a bicubic interpolation that guarantees a close match with the original data.

The axisymmetric component of axial velocity fluctuations is isolated by averaging each snapshot in the azimuthal direction. The cross-spectral density (CSD) matrix between all resulting $(N_x \times N_r) = (15 \times 64)$ spatial positions is then constructed using Welch's periodogram method, with data blocks of 128 time samples, overlapped by 50% (see Ref. [31] for further details). This empirically constructed matrix converges statistically toward the true CSD, which is defined as the covariance of the Fourier-transformed velocity signal $\hat{y}(\mathbf{x}_i, \omega)$,

$$P_{\hat{y}\hat{y}}|_{ij}(\omega) = \mathscr{E}[\hat{y}(\mathbf{x}_i, \omega)\hat{y}^*(\mathbf{x}_j, \omega)]. \tag{14}$$

The "expected value" operator $\mathscr{E}$ denotes the asymptotic limit of an ensemble average. In the present calculations, for numerical reasons, each element of the CSD matrix is further scaled with a factor
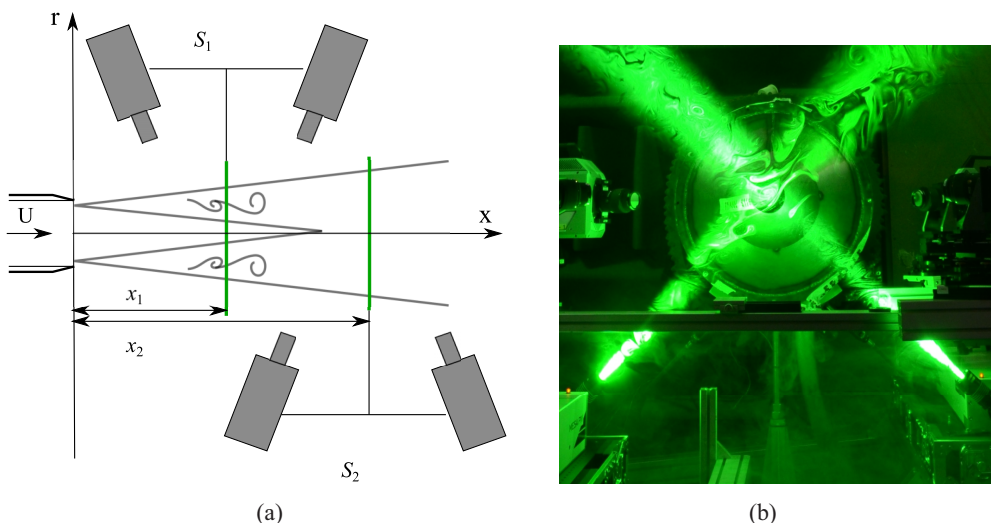
FIG. 11. (a) Sketch of the experimental setup, viewed from the top. The green lines represent the laser light sheets S_1 and S_2, placed at x_1 and x_2, respectively; these planes are shifted during the experiment in the range $x = [1, 8]$ (see Ref. [31]). (b) Front view of the experiment during the PIV acquisition.

$\sqrt{r_i r_j}$, composed of the radial coordinates of any two points for which the correlation is computed. This procedure ensures that the resulting modified CSD matrix is strictly Hermitian [58].

Eigenvectors $\tilde{\phi}_k$ of the modified matrix are computed. These are then again rescaled in each point as $\phi_k(r, x) = \tilde{\phi}_k(r, x) r^{-0.5}$, and they are sorted in descending order of their associated eigenvalues. The structures $\phi_k(r, x)$ represent the SPOD modes, in the terminology of Picard and Delville [11], and as used in recent literature [20,21]. Unfortunately, the same name is also used by Sieber *et al.* [12] for a different modal decomposition, which is not employed here.

The statistical convergence of SPOD modes is examined by dividing the datasets into two blocks, indicated as $i = (1, 2)$, and performing the computation procedure on each subset. Each block corresponds to half of the original dataset. We use a normalized scalar product α between each mode $\phi_{i,k}$ obtained with half of the original dataset and the corresponding mode ϕ_k obtained with the complete set,

$$\alpha_{i,k} = \frac{\langle \phi_k, \phi_{i,k} \rangle}{\sqrt{||\phi_k||_2 \cdot ||\phi_{i,k}||_2}}. \tag{15}$$

The scalar quantity $\alpha_{i,k}$ is the correlation coefficient between the kth mode of subset i and the corresponding mode of the full dataset. We consider modes with a correlation coefficient close to unity as being converged, showing thus that the same computation with half of the dataset leads to a very similar result.

The correlation coefficients for St $= 0.2$, 0.4, 0.6, and 0.8 are presented in Fig. 12. It is clear from these figures that the analysis is rather sensitive to the amount of data being used. The discrepancies in the higher (less energetic) modes are partially explained by differences in the order in which they emerge, depending on the data subset. However, the first two SPOD modes seem to be sufficiently correlated and can be accepted as being converged at all Strouhal numbers below St $= 0.8$. Only modes 1 and 2 will be discussed in the following, for $0.2 \leqslant$ St $\leqslant 0.7$.

B. Resolvent-based modeling of SPOD modes

The relation between resolvent modes, as presented in Sec. III, and SPOD modes, as obtained from the experiments, is made explicit here on the basis of our earlier formulation [19]. The
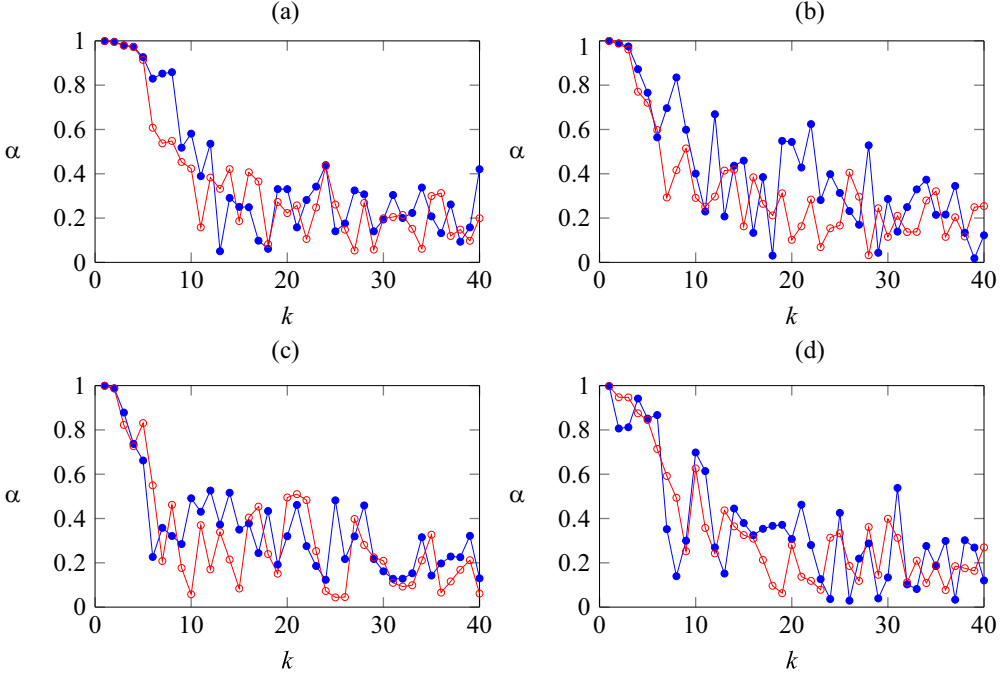
FIG. 12. Correlation coefficients α [Eq. (15)], for a quantification of the statistical convergence of experimental SPOD modes. Two subsets of data are taken from the experimental acquisitions, and for each of these the SPOD modes are computed and compared: ($\bullet$) $\alpha_{1,k}$ and ($\circ$) $\alpha_{2,k}$. Satisfactory convergence is observed at least for mode 1 (throughout) and for mode 2 (at $St < 0.8$). (a) St = 0.2, (b) St = 0.4, (c) St = 0.6, and (d) St = 0.8.

following development is consistent with the recent work of Towne *et al.* [20] and Schmidt *et al.* [21], while using the nomenclature introduced in the previous sections.

Let $f(t)$ and $q'(t)$ represent spatial discretizations of the stochastic forcing and response, as discussed in Sec. III B. The CSD of their spectral components $\hat{f}(\omega)$ and $\hat{q}(\omega)$ is given by

$$P_{\hat{f}\hat{f}}(\omega) = \mathscr{E}[\hat{f}(\omega)\hat{f}^H(\omega)] \quad \text{and} \quad P_{\hat{q}\hat{q}}(\omega) = \mathscr{E}[\hat{q}(\omega)\hat{q}^H(\omega)]. \tag{16}$$

For the purpose of flow modeling, we consider the CSD of an experimentally observable vector $\hat{y}$ of flow quantities,

$$P_{\hat{y}\hat{y}}(\omega) = \mathscr{E}[\hat{y}(\omega)\hat{y}^H(\omega)], \quad \text{with } \hat{y} = C\hat{q}. \tag{17}$$

The relation between $P_{\hat{y}\hat{y}}$ and $P_{\hat{f}\hat{f}}$ at a given frequency involves the resolvent operator; with (11b) and the definitions in Sec. III C, this relation can be written as

$$P_{\hat{y}\hat{y}} = CR\,\mathscr{E}[\hat{f}\hat{f}^H]R^HC^H = CQ\Sigma F^H M P_{\hat{f}\hat{f}} M F\Sigma Q^H C^H. \tag{18}$$

If the forcing $\hat{f}$ is expanded in the basis given by the columns of F, with a coefficient vector β such that $\hat{f} = F\beta$, (18) becomes

$$P_{\hat{y}\hat{y}} = CQ\Sigma P_{\beta\beta}\Sigma Q^H C^H. \tag{19}$$

We now seek the relation between eigenvectors (SPOD modes) of $P_{\hat{y}\hat{y}}$ and the resolvent response modes contained in the matrix Q. If full-state information is available, $C = I$ and $\hat{y} = \hat{q}$, one can write

$$NP_{\hat{y}\hat{y}}N^H = NQ\Sigma P_{\beta\beta}\Sigma Q^H N^H. \tag{20}$$

Recall that the scalar product (8) is represented by the matrix $M = N^H N$. As NQ is unitary, $(NQ)^H NQ = I$, it represents the eigenvector matrix of $N P_{\hat{y}\hat{y}} N^H$, under the condition that $P_{\beta\beta}$ is a diagonal matrix. This condition signifies that the resolvent forcing modes, for a given frequency, are *uncorrelated* in the actual stochastic forcing of the system ("spatial white-noise hypothesis"). It finally follows that Q in this case is the eigenvector matrix of $P_{\hat{y}\hat{y}} M$ (the "weighted CSD" [21]), with the diagonal elements of $P_{\beta\beta} \Sigma^2$ as associated eigenvalues.

If $\hat{y}$ represents only partial-state information, $C \neq I$, such a direct link between resolvent response modes and SPOD modes cannot be made. This is the case for the present experimental dataset. However, under the strong hypothesis $P_{\beta\beta} = I$, it is possible to construct a low-rank approximation

$$P_{\hat{y}\hat{y}} \approx C\tilde{Q}\tilde{\Sigma}^2\tilde{Q}^H C^H \tag{21}$$

of the observable CSD, where $\tilde{Q}$ and $\tilde{\Sigma}$ only contain a limited number of resolvent response modes and associated gains, as obtained from the linear analysis. The eigenvectors of (21), or equivalently the left singular vectors of $C\tilde{Q}\tilde{\Sigma}$, can then be identified and compared to those computed from the experimental data. It may be expected that the leading SPOD mode structure is well represented by such a linear model in situations where the first optimal gain σ_1 is significantly larger than σ_2: as the ratio σ_1/σ_2 tends toward infinity, the leading SPOD mode tends toward the optimal resolvent response mode $C\hat{q}_1$. At finite gain ratios, however, the inclusion of several resolvent modes in $C\tilde{Q}\tilde{\Sigma}$ has the potential to improve the agreement. The comparisons provided in recent analyses of backward-facing step flow [28] and jets [20,21] show such favorable cases of strong gain separation, as discussed in those articles.

C. Comparison between experimental and model results

It is now assessed to what extent the experimentally obtained SPOD modes are accurately reproduced by the resolvent-based model. The success of this comparison depends on many factors, namely, the assumption that our forcing modes are uncorrelated in $P_{\hat{y}\hat{y}}$, the hypotheses involved in the linear resolvent analysis in Sec. III, and the accuracy of both experimental and numerical methods used.

Approximations of $P_{\hat{y}\hat{y}}$ are constructed according to the low-rank model (21). The first five resolvent modes, discussed in Sec. III E, are used to build $\tilde{Q}$ and $\tilde{\Sigma}$ (the low-rank versions of Q and Σ) at various Strouhal numbers. The matrix C selects the streamwise velocity component in the same grid points that are used in the experimental CSDs. SPOD modes are then computed as the left singular modes of the matrix $C\tilde{Q}\tilde{\Sigma}$.

The leading SPOD modes obtained from experimental data and from the resolvent-based model are compared in Fig. 13, for Strouhal numbers St = 0.2, 0.4, 0.6, and 0.7. Contours of their absolute value are shown, and each mode is normalized with respect to its global maximum value. The agreement between experimental (left column) and model results (right column) is remarkably good at Strouhal numbers between 0.4 and 0.7. Within this range of St, maximum SPOD amplitudes are located inside the potential core region of the jet. The maximum along r at each streamwise station follows a line that tends toward the jet axis, evocative of the "critical layer" as discussed by Tissot *et al.* [51]. At St = 0.2, however, the agreement between experiment and model is rather poor. While the experimental mode structure in Fig. 13(a) resembles those found at higher Strouhal numbers, but with its maximum further downstream and possibly outside the measurement window, the resolvent-based model predicts high amplitudes in the outer portion of the shear layer [Figs. 13(b) and 6(a)].

The second SPOD modes are shown in the same manner in Fig. 14. For these modes, the comparison between experimental and model results fails at all Strouhal numbers. Mode structures obtained from the resolvent-based model have high amplitudes inside the shear layer, similar to the suboptimal response structures shown in Fig. 7, whereas the experimentally educed structures are still characterized by maximum amplitudes near the jet axis. Inside the jet, the latter display an amplitude modulation along x with two distinct local maxima. Subsequent SPOD modes show similarly poor agreement, and they are not reported here.
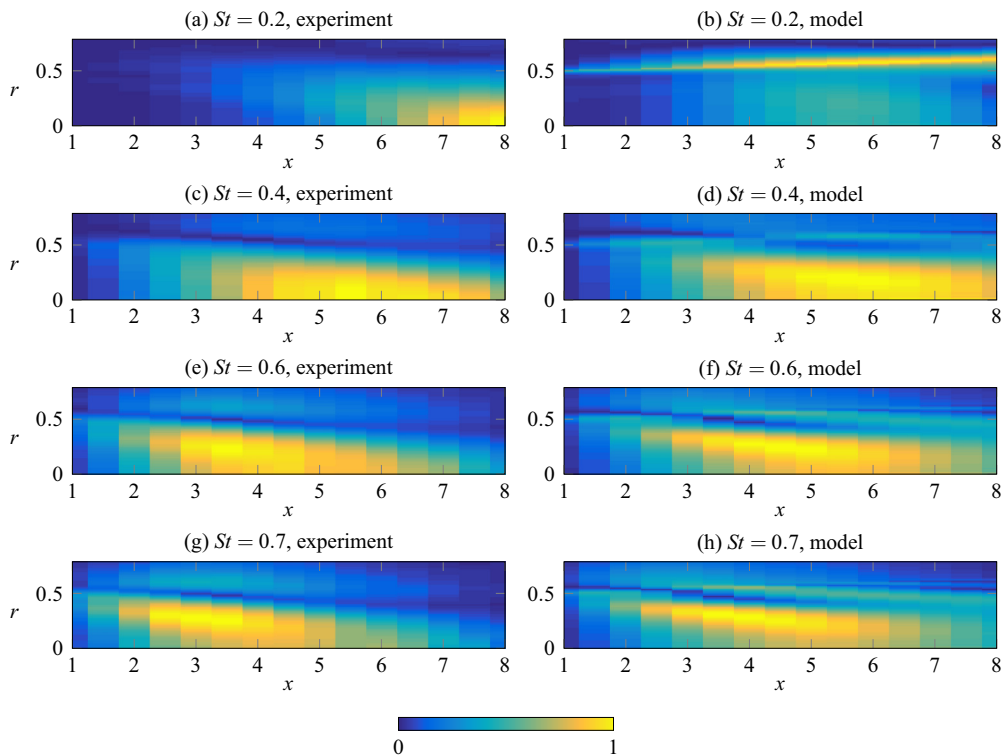
FIG. 13. Modulus of the *first* SPOD mode at St = 0.2, 0.4, 0.6, and 0.7, as obtained from the experimental data (left column) and from the resolvent-based model (right column). The resolution of the color plots corresponds to the spatial grid where the CSD is defined, without interpolation.

Several effects may contribute to the failure of the model to capture the second SPOD mode; a rather obvious one seems to derive from the specific structure of the suboptimal resolvent modes that are included in the low-rank operator (21). The optimal resolvent mode cannot be significantly involved in the second SPOD mode, which is orthogonal to the first one, and none of the four suboptimal structures in Fig. 7 can be expected to reproduce spatial variations of the kind observed in the left column of Fig. 14.

Energy spectra, as given by the eigenvalues of the measured and modelled CSD matrices, are compared in Fig. 15. Their variations with Strouhal number are quite different from one another. The dominant eigenvalue of the experimental CSD takes on its highest value at St = 0.1, and another local maximum arises at St = 0.4. The first and second eigenvalue curves are separated by a factor between 3 and 7 over the interval $0.4 \leqslant \text{St} \leqslant 0.8$, where SPOD modes in model and experiment are in good agreement. CSD eigenvalues derived from the model closely resemble the gain values shown in Fig. 4, with a slight shift of the maximum value from St = 0.7 to 0.6. An important source of discrepancy between the dominant branches in Figs. 15(a) and 15(b) is very likely the assumption that all resolvent forcing modes over all Strouhal numbers are contained in the Reynolds stress fluctuations with *equal amplitude*.

In order to visualise the wave-packet structure of the leading SPOD mode at St = 0.4, the dominant St value according to the experimental spectrum [Fig. 15(a)], the amplitude and the phase of this mode are interpolated onto a fine mesh. This is done both for the experimental and for the model SPOD mode, and the resulting real parts are shown in Figs. 16(a) and 16(b). Clean wave packets are recovered, and their resemblance is even more appreciable than in the amplitude plots of Fig. 13. Recall that the model SPOD mode has been obtained as the eigenmode of a CSD matrix that
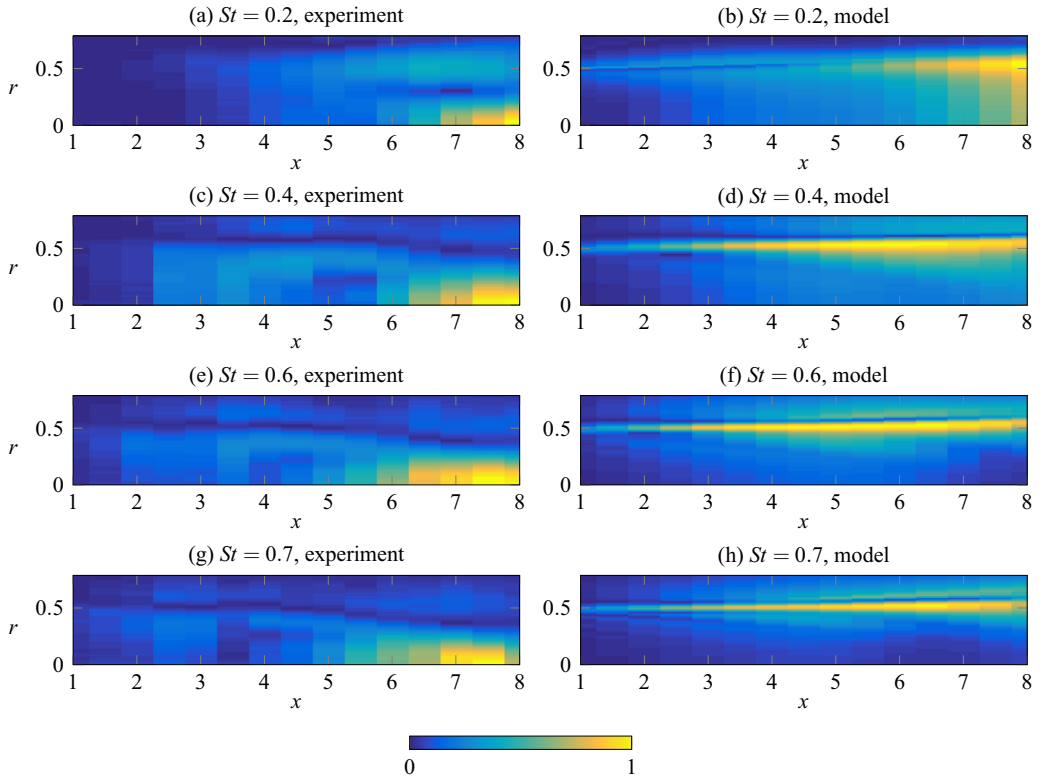
FIG. 14. Modulus of the *second* SPOD mode at St = 0.2, 0.4, 0.6, and 0.7, as obtained from the experimental data (left column) and from the resolvent-based model (right column). The resolution of the color plots corresponds to the spatial grid where the CSD is defined, without interpolation.

was constructed from the first five resolvent response modes at St = 0.4. The optimal response mode alone is plotted in Fig. 16(c); although not strictly identical, it is indeed virtually indistinguishable from the five-mode model result. This comparison demonstrates that the extra effort of including suboptimal response modes in the model has not led to any improvement of the SPOD prediction:
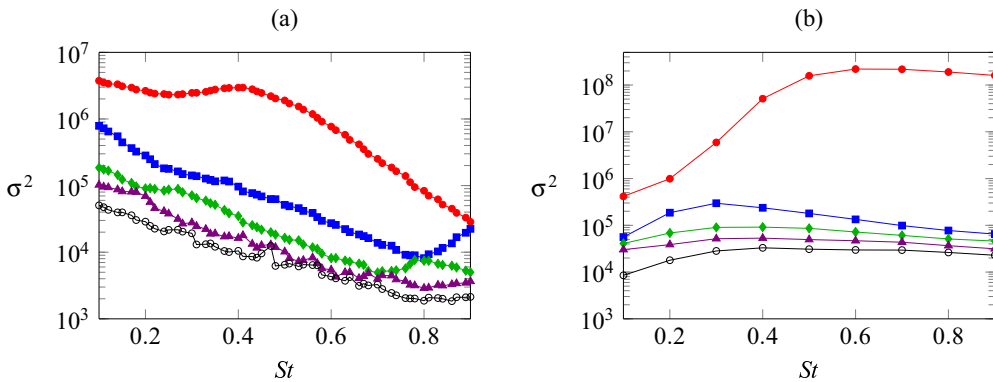

FIG. 15. The leading five CSD eigenvalue branches as functions of Strouhal number (a) from the experiment and (b) from the resolvent-based linear model.
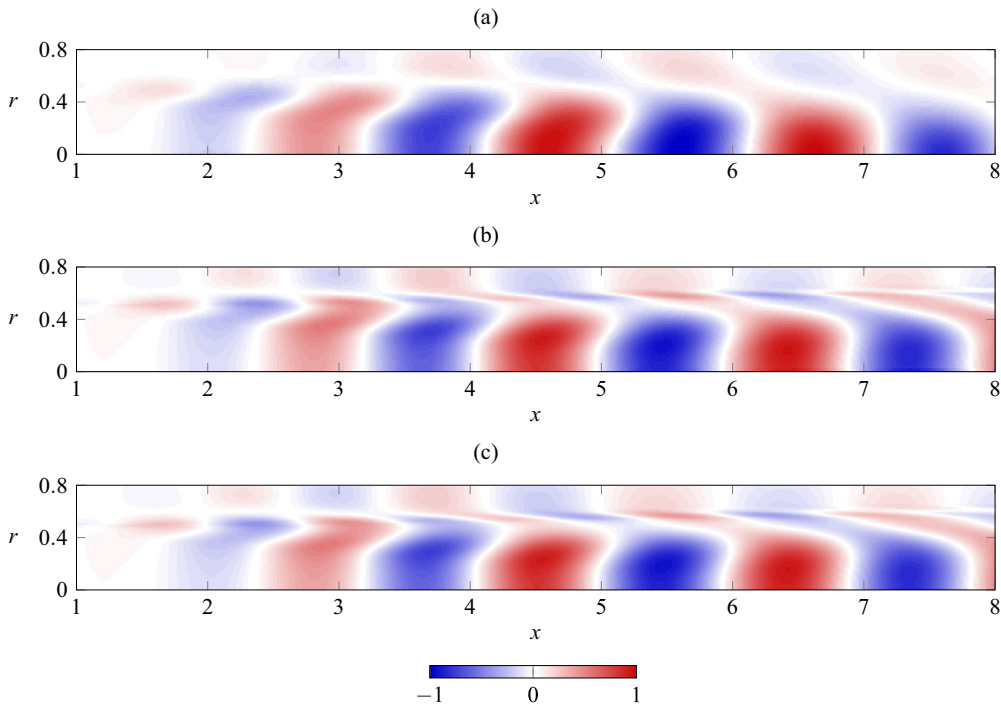
FIG. 16. Interpolated SPOD wave packets at St = 0.4 (a) from the experiment and (b) from the linear model based on five resolvent modes. Amplitude and phase are interpolated between the available data points, and the resulting real part is represented. (c) The corresponding *optimal* response mode alone.

the "rank 1 approximation" used in previous studies [21,28], which consists in equating the optimal response with the first SPOD mode, is applicable in the current jet case, and suboptimal modes are of no use for increasing the accuracy of the linear model.

For a more quantitative comparison, real-part oscillations of the interpolated SPOD modes are extracted along the centerline, and displayed in Fig. 17, together with their amplitude envelope. Black and red lines represent the five-mode model and the experimental data, respectively. Markers indicate the values obtained directly in the original measurement points. Experimental wave packets are traced with their actual absolute amplitude, whereas a best-fit coefficient has been constructed, based on the interval $1 \leqslant x \leqslant 5$, for a proper scaling of the model amplitude. Good agreement is generally observed in the upstream region of exponential amplitude growth; at St = 0.4, the agreement is excellent down to the amplitude maximum. At lower Strouhal numbers, the model underpredicts the maximum, even by a large measure in the case of St = 0.2, whereas at higher Strouhal numbers, the amplitude maximum is overpredicted. Considering that a phase match is imposed in the very first position, $x = 1$, and differences therefore accumulate in the downstream direction, the phase prediction can be said to be satisfactory for all Strouhal numbers above 0.2. Several radial positions have been tested for the present comparison, and all have been found to give very similar agreement. The most notable difference between model and experimental results, at St $\geqslant$ 0.4, is an underpredicted downstream attenuation of fluctuation amplitudes. This trend is clearly visible in Figs. 13, 16, and 17, and it increases with St.

It must be kept in mind that individual wave packets in the present approach are regarded as isolated objects, which is made possible by our choice to replace the nonlinear term with a generic white noise forcing. In reality, all frequencies and azimuthal wave numbers are coupled through the nonlinear Reynolds stresses, such that energy is exchanged between coherent structures,
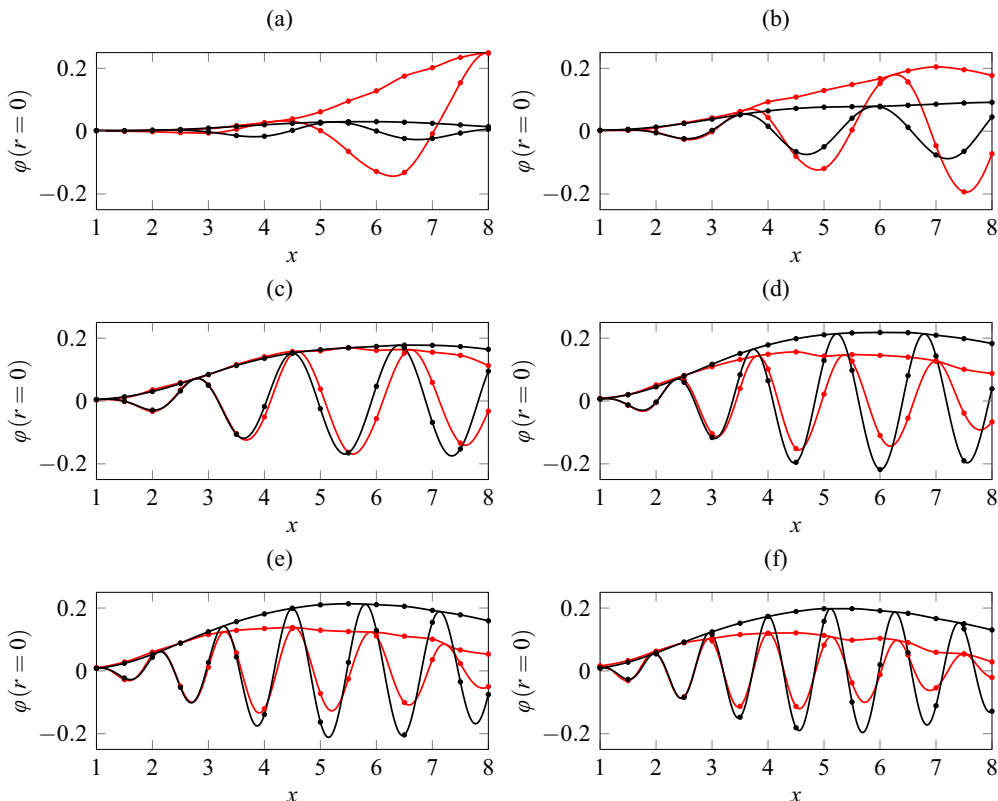
FIG. 17. Comparison between experimental (red) and model (black) SPOD wave packets at various Strouhal numbers. Amplitude and phase variations on the centerline are interpolated between the available data points, indicated by markers. Both the amplitude envelopes and the oscillating real parts are shown. (a) St = 0.2, (b) St = 0.3, (c) St = 0.4, (d) St = 0.5, (e) St = 0.6, and (f) St = 0.7.

axisymmetric and nonaxisymmetric, at different frequencies. This energy transfer would be correctly represented by spatial variations of the forcing at a given Strouhal number, which influence the wave-packet envelope, while furthermore the forcing distributions at all Strouhal numbers are coupled among each other. It remains a challenge for future work to identify a consistent way to model these interactions in a turbulent flow with a broadband spectrum of frequencies and azimuthal wave numbers.

D. Comparison with linear jet studies in the recent literature

The resolvent modes presented in Sec. III E and their comparison with SPOD modes in Sec. V C are, by and large, consistent with the findings of similar recent studies [15,17,18,20,21]. One striking difference with the results of Schmidt *et al.* [21] is noted in the structure of suboptimal response modes: At Strouhal numbers above 0.2, our computations yield a clean separation between modal shear and nonmodal Orr structures, whereas Schmidt *et al.* [21] observe a mixing of shear-induced wave packets with Orr-related structures in all their suboptimals. The associated forcing structures, shown in Figs. 5 and 7, suggest that this difference can be attributed to the presence of a nozzle in our numerical configuration. Forcing inside the pipe is found to be particularly efficient, especially in the case of the optimal resolvent mode, which must therefore be expected to be very sensitive to the truncation of the most receptive flow region. In turn, changes in the optimal mode will be
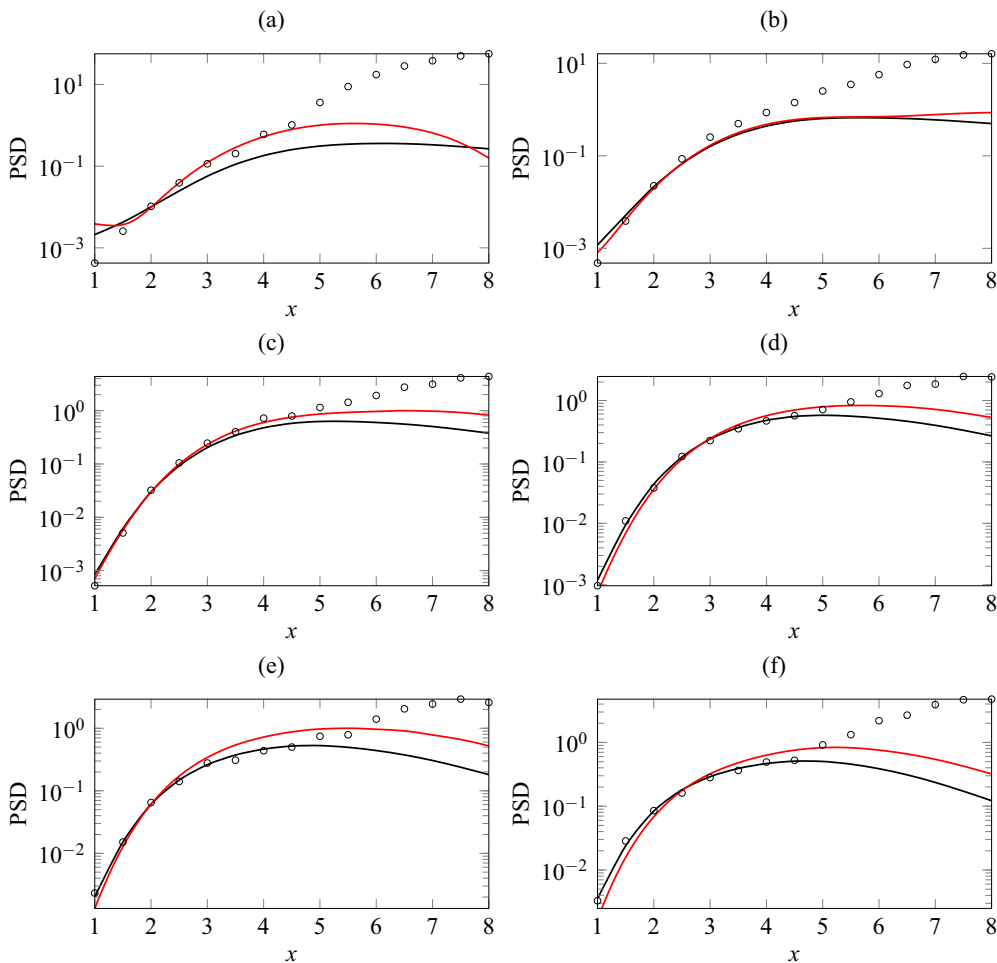
FIG. 18. Power-spectral density (PSD) along the jet centreline as a function of x at different Strouhal numbers. (○) Hot-wire measurements [13]; (–) PSE model [13]; (——) optimal response mode (present calculations). (a) St = 0.2, (b) St = 0.3, (c) St = 0.4, (d) St = 0.5, (e) St = 0.6, and (f) St = 0.7.

accompanied by changes in the orthogonal suboptimals. The localization of optimal forcing in the present results may furthermore be linked to the observed sensitivity of LES statistics with respect to flow details in the nozzle boundary layer [32].

Numerous previous studies addressing the linear modeling of wave packets in turbulent jets, when only *boundary forcing* at the inflow was considered, observed discrepancies in the initial amplitude growth at low Strouhal numbers, typically St $\leqslant$ 0.3 [5,13,59], which play an important role in the generation of jet noise. These differences were initially attributed either to the weakly nonparallel assumption that underlies the parabolized stability equations (PSE) or to unmodeled nonlinear effects. The limitation of PSE with regard to nonparallelism has since been ruled out by computations based on the fully nonparallel, linearized Euler equations [6]. We complete this study by revisiting the low-Strouhal discrepancy in the resolvent framework, where *volume forcing* is included as a surrogate for nonlinear effects.

Figure 18 compares the PSE and measured power-spectral density (PSD) results from Cavalieri *et al.* [13] with the kinetic energy of the optimal response modes presented in Sec. III E. All curves are extracted on the jet axis. It can be seen how, at St = 0.2, the resolvent mode captures the

initial wave-packet growth measured in the experiment, and underpredicted by PSE, while at higher Strouhal numbers the PSE solution and resolvent mode comprise similar initial growth. The optimal forcing at St = 0.2 [Figs. 5(a) and 5(b)] involves significant contributions from inside the shear layer of the free jet, which were excluded in the models of Refs. [5,6,13,59]. This volume forcing boosts the spatial growth of the response wave packet near the nozzle. Although the high-amplitude portion of the optimal response mode is not in agreement with the experimental PSD, the initial growth is faithfully reproduced. This observation suggests that Orr-type forcing through Reynolds stresses in the free shear layer indeed contributes to perturbation growth at low Strouhal number near the nozzle.

Another much-discussed discrepancy between PSE and PSD results arises in the downstream region where linear models predict a decay in perturbation amplitude, whereas the PSD displays a marked additional growth, accompanied by a slope break in the growth rate. Jordan *et al.* [60] interpret the PSD growth in this region in terms of the non-normality of decaying local eigenmodes. However, this peculiar behavior of the PSD is entirely absent in the present SPOD results, in agreement with the LES-based analysis by Schmidt *et al.* [21]. This leads us to conclude that the spatiotemporal coherence, from which SPOD modes are derived, provides a sharper and more pertinent criterion for the eduction of coherent turbulent structures than the PSD, which only measures temporal coherence. As discussed by Towne *et al.* [20], the PSD may contain the trace of many SPOD modes. Figure 18 strongly suggests that suboptimal SPOD or resolvent mode wave packets contribute in a very significant way to the turbulent dynamics downstream of $x = 4$. The Orr-type character of our suboptimal resolvent modes is fully consistent with the discussion of the PSD behavior by Tissot *et al.* [51].

VI. CONCLUSIONS

Perturbation wave packets in the mean flow of a turbulent jet have been computed in the form of resolvent modes. Nonlinear terms in the governing equations, which arise in the form of generalized Reynolds stresses, are regarded as generic forcing terms [22,28,38]. The five leading orthogonal forcing-response modes have been identified for several values of the Strouhal number between 0.2 and 1.5. The most amplified ("optimal") mode, over the interval $0.3 \leqslant \text{St} \leqslant 1.5$, bears the traits of a shear instability in the free jet, with strong spatial growth in the potential core. This mode arises principally from forcing in the nozzle boundary layer, which takes the shape of tilted structures indicative of the Orr mechanism, as described in our earlier studies [15,18]. The dominant role of shear instability in the free-jet portion of the optimal resolvent mode has been demonstrated by projecting the response wave packet onto a local k^+ shear instability mode. Subsequent ("suboptimal") modes, with significantly lower energy gain, appear to exploit the Orr mechanism in the free jet. This interpretation is supported via an analogy with optimal forcing in a fully developed parallel jet. At low Strouhal number, St = 0.2, both shear and Orr mechanisms in the free jet seem to contribute to the optimal resolvent mode in a mixed fashion.

Coherent structures have then been extracted from experimental measurements, in the form of eigenvectors of the cross-spectral density, named "spectral POD" (SPOD) modes [11,20]. Following recent works [19,20], it has been demonstrated that such modes should, in theory, correspond to the optimal response mode described above, under two strong conditions: (i) the corresponding optimal forcing modes are statistically *uncorrelated* among each other in the nonlinear dynamics, which are interpreted in the linear model as forcing terms; (ii) the SPOD modes are extracted from *full-state* information. As full-state information is not available from the experimental dataset, the five leading response modes were instead used to construct a low-rank model of the cross-spectral density, under the even stronger assumption that the corresponding optimal forcing structures are uncorrelated and of *equal amplitude* in the nonlinear dynamics. This procedure constitutes our resolvent-based linear model for the statistical dynamics of coherent turbulence structures, as characterised by two-point covariance.

Very good agreement has been found between the leading SPOD modes as obtained from the experiment and from the resolvent-based model, in a range of Strouhal numbers around 0.4. The leading SPOD mode of the linear model is in fact nearly identical to the optimal response wave packet, such that the intermediate step of building a model CSD from several response structures turned out to be unimportant for the comparison with the experiment. At $St = 0.4$, the model reproduces accurately both the amplitude variations over three decades, down to at least 7 diameters behind the nozzle, and the phase variations in the experimentally extracted SPOD mode. The maximum wave-packet amplitude is underpredicted at $St < 0.4$ and overpredicted at $St > 0.4$. At all Strouhal numbers between 0.2 and 0.7, the initial streamwise perturbation growth close to the nozzle is very well retrieved.

Subsequent (nonleading) SPOD modes of the experimental data and the linear model do not show satisfactory agreement. The discussion of their discrepancies may be approached from two ends: On the one hand, the linear model probably cannot replicate the experimental results because of the restricted number of basis vectors and because the above-mentioned modeling hypotheses are too crude in order to reproduce the dynamics beyond leading order. On the other hand, the experimental measurements may be too sparse, particularly in terms of spatial resolution, in order to detect the rather fine-scale structures that the linear model predicts.

In summary, the results presented in this paper demonstrate that linear resolvent analysis, performed around the spatially developing, time-averaged mean flow, represents a valid tool for the modeling of coherent wave-packet structures in a stochastically driven turbulent jet. Only the mean flow is required for the construction of this linear model. Wave packets arising from shear instability, which experience the strongest energy gain, could be matched between model and experiment at Strouhal numbers between 0.2 and 0.7. While these general conclusions corroborate those of the parallel study by Schmidt *et al.* [21], performed on the basis of LES data for the same flow configuration, differences are observed in the resolvent mode structures. These relate to the separation of shear and Orr mechanisms in the optimal and suboptimal modes, and they are attributed to the inclusion of a nozzle in the present analysis.

From a final comparison with earlier PSD measurements [13], it is inferred that suboptimal SPOD modes seem to play a determining role near and beyond the end of the potential core region. While the link between these modes and free-jet Orr-type growth mechanisms is one more time predicted by the present analysis, poor agreement is found between suboptimal structures in model and experiment. Further progress of wave-packet modeling in high-Reynolds-number turbulent jets requires establishing the dynamics that dominate in the flow region downstream of the potential core and how best to model them.

[1] P. Jordan and T. Colonius, Wave packets and turbulent jet noise, Annu. Rev. Fluid Mech. **45**, 173 (2013).

[2] A. Michalke, Instabilität eines kompressiblen runden Freistrahls unter Berücksichtigung des Einflusses der Strahlgrenzschichtdicke, Z. Flugwiss. **19**, 319 (1971).

[3] D. G. Crighton and M. Gaster, Stability of slowly diverging jet flow, J. Fluid Mech. **77**, 397 (1976).

[4] K. Oberleithner, L. Rukes, and J. Soria, Mean flow stability analysis of oscillating jet experiments, J. Fluid Mech. **757**, 1 (2014).

[5] K. Gudmundsson and T. Colonius, Instability wave models for the near-field fluctuations of turbulent jets, J. Fluid Mech. **689**, 97 (2011).

[6] Y. B. Baqui, A. Agarwal, A. V. G. Cavalieri, and S. Sinayoko, A coherence-matched linear source mechanism for subsonic jet noise, J. Fluid Mech. **776**, 235 (2015).

[7] B. F. Farrell and P. J. Ioannou, Stochastic forcing of the linearized Navier-Stokes equations, Phys. Fluids A **5**, 2600 (1993).

[8] B. F. Farrell and P. J. Ioannou, Statistical state dynamics: A new perspective on turbulence in shear flow, arXiv:1412.8290.

[9] P. J. Schmid, Nonmodal stability theory, Annu. Rev. Fluid Mech. **39**, 129 (2007).

[10] S. Bagheri, D. S. Henningson, J. Hoepffner, and P. J. Schmid, Input-output analysis and control design applied to a linear model of spatially developing flows, Appl. Mech. Rev. **62**, 020803 (2009).

[11] C. Picard and J. Delville, Pressure velocity coupling in a subsonic round jet, Int. J. Heat Fluid Fl. **21**, 359 (2000).

[12] M. Sieber, C. O. Paschereit, and K. Oberleithner, Spectral proper orthogonal decomposition, J. Fluid Mech. **792**, 798 (2016).

[13] A. V. G. Cavalieri, D. Rodriguez, P. Jordan, T. Colonius, and Y. Gervais, Wavepackets in the velocity field of turbulent jets, J. Fluid Mech. **730**, 559 (2013).

[14] D. Rodriguez, A. V. G. Cavalieri, T. Colonius, and P. Jordan, A study of linear wavepacket models for subsonic turbulent jets using local eigenmode decomposition of PIV data, Eur. J. Mech. B/Fluids B **49**, 308 (2015).

[15] X. Garnaud, L. Lesshafft, P. J. Schmid, and P. Huerre, The preferred mode of incompressible jets: Linear frequency response analysis, J. Fluid Mech. **716**, 189 (2013).

[16] X. Garnaud, R. D. Sandberg, and L. Lesshafft, Global response to forcing in a subsonic jet: Instability wavepackets and acoustic radiation, AIAA Paper 2013-4633 (2013).

[17] J. Jeun, J. W. Nichols, and M. R. Jovanović, Input-output analysis of high-speed axisymmetric isothermal jet noise, Phys. Fluids **28**, 047101 (2016).

[18] O. Semeraro, L. Lesshafft, V. Jaunet, and P. Jordan, Modeling of coherent structures in a turbulent jet as global linear instability wavepackets: Theory and experiment, Int. J. Heat Fluid Fl. **62**, 24 (2016).

[19] O. Semeraro, V. Jaunet, P. Jordan, A. V. G. Cavalieri, and L. Lesshafft, Stochastic and harmonic optimal forcing in subsonic jets, AIAA Paper 2016-2935 (2016).

[20] A. Towne, O. T. Schmidt, and T. Colonius, Spectral proper orthogonal decomposition and its relationship to dynamic mode decomposition and resolvent analysis, J. Fluid Mech. **847**, 821 (2018).

[21] O. T. Schmidt, A. Towne, G. Rigas, T. Colonius, and G. A. Brès, Spectral analysis of jet turbulence, J. Fluid Mech. **855**, 953 (2018).

[22] B. F. Farrell and P. J. Ioannou, Generalized stability theory. part I: Autonomous operators, J. Atmos. Sci. **53**, 2025 (1996).

[23] F. Alizard, S. Cherubini, and J.-C. Robinet, Sensitivity and optimal forcing response in separated boundary layer flows, Phys. Fluids **21**, 064108 (2009).

[24] A. Monokrousos, E. Åkervik, L. Brandt, and D. S. Henningson, Global three-dimensional optimal disturbances in the Blasius boundary-layer flow using time-steppers, J. Fluid Mech. **650**, 181 (2010).

[25] D. Sipp and O. Marquet, Characterization of noise amplifiers with global singular modes: The case of the leading-edge flat-plate boundary layer, Theor. Comp. Fluid Dyn. **27**, 617 (2013).

[26] G. Dergham, D. Sipp, and J.-C. Robinet, Stochastic dynamics and model reduction of amplifier flows: The backward facing step flow, J. Fluid Mech. **719**, 406 (2013).

[27] E. Boujo and F. Gallaire, Sensitivity and open-loop control of stochastic response in a noise amplifier flow: The backward-facing step, J. Fluid Mech. **762**, 361 (2015).

[28] S. Beneddine, D. Sipp, A. Arnault, J. Dandois, and L. Lesshafft, Conditions for validity of mean flow stability analysis, J. Fluid Mech. **798**, 485 (2016).

[29] A. Towne, T. Colonius, P. Jordan, A. V. G. Cavalieri, and G. A. Brès, Stochastic and nonlinear forcing of wavepackets in a Mach 0.9 jet, AIAA Paper 2015-2217 (2015).

[30] A. V. G. Cavalieri, P. Jordan, and L. Lesshafft, Wave-packet models for jet dynamics and sound radiation, Appl. Mech. Rev. **71**, 020802 (2019).

[31] V. Jaunet, P. Jordan, and A. V. G. Cavalieri, Two-point coherence of wave packets in turbulent jets, Phys. Rev. Fluids **2**, 024604 (2017).

[32] G. A. Brès, P. Jordan, V. Jaunet, M. Le Rallic, A. V. G. Cavalieri, A. Towne, S. K. Lele, T. Colonius, and O. T. Schmidt, Importance of the nozzle-exit boundary-layer state in subsonic turbulent jets, J. Fluid Mech. **851**, 83 (2018).

[33] See Supplemental Material at http://link.aps.org/supplemental/10.1103/PhysRevFluids.4.063901 for the mean flow file.

[34] S. B. Pope, *Turbulent Flows* (Cambridge University Press, Cambridge, UK, 2000).

[35] X. Garnaud, Modes, transient dynamics, and forced response of circular jets, Ph.D. thesis, Ecole polytechnique, Palaiseau, France, 2012.

[36] R. D. Sandberg, Governing equations for a new compressible Navier-Stokes solver in general cylindrical coordinates, Monograph No. AFM-07/07, School of Engineering Sciences, University of Southampton, 2007 (unpublished).

[37] W. C. Reynolds and A. K. M. F. Hussain, The mechanics of an organized wave in turbulent shear flow. Part 3. Theoretical models and comparisons with experiments, J. Fluid Mech. **54**, 263 (1972).

[38] B. J. McKeon and A. S. Sharma, A critical-layer framework for turbulent pipe flow, J. Fluid Mech. **658**, 336 (2010).

[39] O. Tammisola and M. P. Juniper, Coherent structures in a swirl injector at Re = 4800 by nonlinear simulations and linear global modes, J. Fluid Mech. **792**, 620 (2016).

[40] K. Oberleithner, M. Stöhr, S. H. Im, C. M. Arndt, and A. M. Steinberg, Formation and flame-induced suppression of the precessing vortex core in a swirl combustor: Experiments and linear stability analysis, Combust. Flame **162**, 3100 (2015).

[41] O. Semeraro, L. Lesshafft, and R. D. Sandberg, Can jet noise be predicted using linear instability wavepackets? in *Proceedings of the 5th International Conference on Jets, Wakes and Separated Flows* (Springer, Berlin, 2016), pp. 413–418.

[42] E. Åkervik, U. Ehrenstein, F. Gallaire, and D. S. Henningson, Global two-dimensional stability measures of the flat plate boundary-layer flow, Eur. J. Mech. B/Fluids **27**, 501 (2008).

[43] P. Huerre and P. Monkewitz, Local and global instabilities in spatially developing flows, Annu. Rev. Fluid Mech. **22**, 473 (1990).

[44] X. Garnaud, L. Lesshafft, P. J. Schmid, and P. Huerre, Modal and transient dynamics of jet flows, Phys. Fluids **25**, 044103 (2013).

[45] B.-T. Chu, On the energy transfer to small disturbances in fluid flow (part I), Acta Mech. **1**, 215 (1965).

[46] V. Hernandez, J. E. Roman, and V. Vidal, SLEPc: A scalable and flexible toolkit for the solution of eigenvalue problems, ACM Trans. Math. Software (TOMS) **31**, 351 (2005).

[47] M. Fosas de Pando, D. Sipp, and P. J. Schmid, Efficient evaluation of the direct and adjoint linearized dynamics from compressible flow solvers, J. Comput. Phys. **231**, 7739 (2012).

[48] J. Berland, C. Bogey, O. Marsden, and C. Bailly, High-order, low dispersive, and low dissipative explicit schemes for multiple-scale and boundary problems, J. Comput. Phys. **224**, 637 (2007).

[49] T. J. Poinsot and S. K. Lele, Boundary conditions for direct simulations of compressible viscous flows, J. Comput. Phys. **101**, 104 (1992).

[50] T. Colonius, Modeling artificial boundary conditions for compressible flow, Annu. Rev. Fluid Mech. **36**, 315 (2004).

[51] G. Tissot, M. Zhang, F. Lajus, A. V. G. Cavalieri, P. Jordan, and T. Colonius, Sensitivity of wavepackets in jets to non-linear effects: The role of the critical layer, J. Fluid Mech. **811**, 95 (2017).

[52] G. Tissot, F. Lajús, A. V. G. Cavalieri, and P. Jordan, Wave packets and Orr mechanism in turbulent jets, Phys. Rev. Fluids **2**, 093901 (2017).

[53] K. M. Butler and B. F. Farrell, Three-dimensional optimal perturbations in viscous shear flow, Phys. Fluids A **4**, 1637 (1992).

[54] J. Jiménez, How linear is wall-bounded turbulence? Phys. Fluids **25**, 110814 (2013).

[55] L. Lesshafft and P. Huerre, Linear impulse response in hot round jets, Phys. Fluids **19**, 024102 (2007).

[56] S. Le Dizès, P. A. Monkewitz, and P. Huerre, Viscous structure of plane waves in spatially developing shear flows, Phys. Fluids **7**, 1337 (1995).

[57] L. Lesshafft, Artificial eigenmodes in truncated flow domains, Theor. Comput. Fluid Dyn. **32**, 245 (2018).

[58] J. H. Citriniti and W. K. George, Reconstruction of the global velocity field in the axisymmetric mixing layer utilizing the proper orthogonal decomposition, J. Fluid Mech. **418**, 137 (2000).

[59] D. E. Breakey, P. Jordan, A. V. G. Cavalieri, and O. Léon, Near-field wavepackets and the far-field sound of a subsonic jet, AIAA Paper 2013-2083 (2013).

[60] P. Jordan, M. Zhang, G. Lehnasch, and A. V. G. Cavalieri, Modal and non-modal linear wavepacket dynamics in turbulent jets, AIAA Paper 2017-3379 (2017).